Automatic Geolocation and Measuring of Offshore Energy Infrastructure with Multimodal Satellite Data

Ping Ma, Malcolm Macdonald, *Member, IEEE*, Sally Rouse, and Jinchang Ren, *Senior Member*, *IEEE*

***Abstract*—With increasing trend of energy transition to low carbon economies, the rate of offshore structure installation and removal will rapidly accelerate through offshore renewable energy development and oil and gas decommissioning. Knowledge of the location and size of offshore infrastructure is vital in management of marine ecosystems, and also for safe navigation at sea. The availability of multimodal data enables the systematic assessment of offshore infrastructure. In this paper, we propose an automatic solution for the geolocation and size evaluation of offshore infrastructure through a data fusion model of Sentinel-1 Synthetic Aperture Radar (SAR) data and Sentinel-2 Multi-Spectral Instrument (MSI) imagery. The use of the Sentinel-1 (SAR) data aims to quick localization of the candidate offshore energy infrastructure by its all-weather imaging capabilities, while the high-resolution optical data provided by the Sentinel-2 can enable more accurate localization and measurement of the offshore infrastructure. To be specific, a candidate detection model is applied to a time-series of Sentinel-1 images to extract the 'guided area' of the infrastructure, followed by morphological operation based precise localization within an individual Sentinel-2 image as well as estimating the size of each structure. With validation against the ground truth data of the Scottish waters from the baseline and closing bays, to the limit of the Exclusive Economic Zone of Scotland, an area of 371,915 km^2, our method has automatically identified 332 objects with an omission error of 0.3% and a commission rate of 0%. Our proposed method was comprehensively compared to two state-of-the-art offshore energy infrastructure detection algorithms. The results validate that our method achieves the highest overall accuracy of 99.70%, surpassing the compared methods by 3.84-12.50%. For the size evaluation, the achieved mean topside area size error of oil/gas platforms and the mean error for diameter length measurement of wind turbines both are 1 pixel in Sentinel-2 images, providing an effective technique for the identification and estimation of offshore infrastructure.**

***Index Terms*—Offshore oil/gas platforms, Offshore wind turbines, Multimodal satellite data, Size assessment.**

This work was supported by the SAGES-MASTS Policy Internship organized by Marine Scotland Science, the University of Strathclyde JARA Scholarship and the PhD Scholarship of the China Scholarship Council. Corresponding author: J. Ren (jinchang.ren@ieee.org).

P. Ma, J. Ren are with National Subsea Centre, Robert Gordon University, Aberdeen, United Kingdom.

M. Macdonald is with the Applied Space Technology Laboratory, Centre for Signal & Image Processing, Department of Electronic and Electrical Engineering, University of Strathclyde, Glasgow, United Kingdom.

S. Rouse is with the Offshore Energy Environmental Advice Group, Marine Scotland Science, Aberdeen, United Kingdom.

I. INTRODUCTION

THE introduction of engineered structures to the marine environment can have profound effects on the ecosystems, including through interactions with oceanographic processes, biological productivity and the spatial distribution of fish, mammals, and birds [1], [2]. Authorities, in different countries, such as the global marine science community, governments/regulators and operators are actively seeking greater international alignment on installation and removal practices as well as policies for offshore infrastructure to ensure their impacts to the marine environment are minimized. This requires accurate and accessible knowledge on structures, especially their quantity, spatial distribution, and size.

Globally, energy infrastructure including oil and gas platforms, and wind turbines constitute a substantial proportion of offshore structures [3], [4]. Many countries maintain databases of offshore energy structures. However, many of these databases have restricted access, inaccurate data, omissions, and/or lack of up-to-date information [5], [6]. Moreover, oil and gas production platforms can be relocated, creating a risk to safe navigation of shipping if nautical charts are not promptly updated with new location data. Thus, it is highly demanding to develop a method to quickly and accurately detect the location and properties (e.g., size, shape, type, structural details) of offshore infrastructure. Although there are many conventional survey approaches which can provide highly accurate detection, they are generally unsuitable for deployment at the global scale due to the high degree of time and cost requirements [7]. With the advancement of space-based remote sensing technologies, a wide range of satellite data is now being acquired from diverse sensors, leading to the emergence of multimodal satellite data. As different modalities of data may provide supplementary information to each other, such as various coverage and imaging conditions, the combination of them can help to achieve more robust and accurate detection and measurements [8]. These data have the capabilities of short revisit periods, low cost and synchronous observations in larger areas [9], [10]. The synchronous observation refers to the capability of satellites to capture the data simultaneously or nearly simultaneously over a large area [11]. Such capabilities will allow for the timely identification and understanding of the dynamic changes in the large observed area, offering a great potential for efficient and effective monitoring of the offshore energy infrastructure.

For the observation of offshore energy infrastructure, satellites offer a frequently updated, and archived, near-global database. For example, Liu et al. [7] proposed an automatic method with the Landsat-8 OLI (band 6) for the detection of offshore platforms in Persian Gulf, the Gulf of Mexico and the Gulf of Thailand. This method considers the features of spectra, texture, size, location and shape to discriminate the platforms from ocean background. In Zhao et al. [12], offshore oil/gas platforms in the South China Sea are identified using the Landsat optical images, using multiple sliding windows with dynamic thresholds to recognize candidate objects. Followed by laminating, three images of consecutive periods are combined or layered to label interested objects e.g., oil/gas platforms only when their presence are confirmed in all the three images. In order to improve the platform detection accuracy with a single image, Zhu et al. [13] employed the Harris detector and intensity-texture feature image

to extract the platforms from a Sentinel-2 L2A Image in Persian Gulf of Mexico area. Xu et al. [14] developed a visual saliency detection approach determine the status of offshore wind turbines in the North Sea and surrounding waters, based on time-series of multi-source optical satellite images including Landsat-5 Thematic Mapper (TM), Landsat-7 Thematic Mapper Plus (ETM+), Landsat-8 Operational Land Imager (OLI), and Sentinel-2 Multi-Spectral Instrument (MSI). Zhu et al. [15] proposed an automatic method for offshore platforms identification on the Landsat 7 ETM+ images in Caspian Sea area, where a cloud shadow-free Normalized Difference Water Index (NDWI) composite was built with multiple threshold segmentation to remove the influence of cloud and extract drilling rigs. Strikingly, all these methods employed optical imagery and so suffered from cloud contamination, which can significantly reduce the number of available images for object detection.

The high temperature and brightness of waste gas flames at night have also been used for the identification and monitoring of oil and gas platforms. Croft [16] firstly used the DMSP/OLS night-time light image data to identify the waste gas flame. Casadio et al. [17] monitored the night-time gas flaring activity of the extracted offshore oil/gas platforms in the North Sea area through the fusion of the Synthetic Aperture Radar (SAR) and Along Track Scanning Radiometer (ATSR) data. The positions of rigs are firstly extracted by SAR data, and then flaring activity is estimated on the short-wave infrared band (1.6 μm) at ATSR. Anejionu et al. [18] developed a double threshold segmentation approach for the retrieval of the flaring location and the volume of gas combusted in the Niger Delta from 2000 to 2014 through nighttime Moderate-resolution Imaging Spectroradiometer (MODIS) thermal imagery. Elvidge et al. [19] further refined the network function virtualization (VNF) algorithm [20] to extract global waste gas combustion sources based on the thermal anomalies with high-resolution National Polar-orbiting Operational Environmental Satellite System Preparatory Project/Visible infrared Imaging Radiometer (NPP/VIIRS) images. Some, but not all, of these methods resolve the issue of cloud contamination however they are only applicable to platforms with gas combustion, and therefore not able to detect the full suite of energy infrastructure in the marine environment.

Given the capabilities to image through cloud, and in darkness, SAR can overcome the shortcomings of optical imagery. For example, Cheng et al. [21] extracted offshore oil/gas platforms from multitemporal ENVISAT ASAR data by a two-parameter Constant False Alarm Rate (CFAR) detector. Wong et al. [6] detected offshore infrastructure including oil platforms or platform complexes and wind turbines by using multi-temporal SAR and Google Earth Engine, in which the median composite, Gaussian difference, thresholding and morphological post processing are adopted. An et al. [22] proposed an iterative cell averaging CFAR method to detect the offshore wind turbines and oil rigs by monitoring the stationariness of marine targets on strict time-series of GF-3 and RADARSAT-2 SAR data. Nunziata et al. [23] developed a dual-polarimetric model utilizing X-band COSMO-SkyMed PingPong mode SAR data for metallic target observation, employing a correlation-based approach and a CFAR method. Xu et al. [24] introduced a machine learning based approach for dynamic detection of offshore wind turbines from Sentinel-1 SAR data, which includes cumulatively averaging operator, a refined Lee filter and CFAR technique for noise

reduction, a random forest (RF) model trained on the Google Earth Engine (GEE) platform, and mathematical morphology-based spatial data differentiation for monitoring wind turbine changes, demonstrating high accuracy and potential for global offshore wind turbine detection. Liu et al. [25] presented a time-series remote sensing approach (TSRS) for detecting offshore oil/gas platforms on multi-source optical and SAR images. The method employed a stepwise optimization strategy to mitigate noise and a cross geo-correction strategy using high-geometric accuracy images to rectify poorly geo-referenced images. Marino et al. [26] proposed a multipolarization model to analyze the backscattering behavior of offshore platforms using dual-polarization X-band SAR imagery, aiming to address the challenge of reduced copolarized backscattered intensity under low incidence angles. Liu et al. [27] developed a novel method for the detection of global offshore oil/gas platforms by using the position-invariant characteristic, which aims to systematically evaluate the geometric location accuracy of medium-resolution remote sensing data on ocean scenes. This study validated that the data from the Sentinel-1, Sentinel-2, ENVISAT and ALOS-1 have higher geometric accuracy than those from the JERS-1 and RADARDAT-1. Zhang et al. [3] created a global offshore wind turbine database using the Sentinel-1 SAR time-series images spanning from 2015 to 2019. Through the utilization of a percentile-based annual SAR image reduction and auto-adaptive thresholding algorithm implemented on the GEE platform, the geolocations of worldwide offshore wind turbines are successfully identified. Hoeser et al. [29] introduced the Deep-learning-derived Offshore Wind Turbines (DeepOWT) dataset, a global-scale open-access dataset utilizing Sentinel-1 SAR data, along with deep-learning-based object detection using two cascading convolutional neural networks (CNNs). This dataset provides information on the deployment stages of offshore wind energy infrastructure with a quarterly frequency spanning from July 2016 to June 2021.

Although these studies have presented ways for geolocating of the offshore energy infrastructure, most of them fail to offer more detailed analysis in terms of accurate location and size measurement of different types of infrastructure. In this paper, an automatic geolocating and measuring approach of offshore energy infrastructure is proposed by combining the strengths of both the Sentinel-1 SAR and Sentinel-2 Multi-Spectral Instrument (MSI) images. To quickly geolocate the offshore energy infrastructure, the inherent capacity of SAR to mitigate the impact of adverse weather conditions is utilized. The time-series Sentinel-1 data in conjunction with temporal background modeling and 2D-singular Spectrum Analysis (SSA) filtering are employed to first detect the candidate regions of interests as potential objects, referred to ‘guided area’. The geolocation is then further refined by employing the proposed spectral-spatial method, namely RGB (red (R), green (G) and blue (B) bands) fused morphological reconstruction on the Sentinel-2 MSI data. In order to measure the offshore energy infrastructure, a size estimation model is subsequently introduced. Specifically, a novel classification method is introduced, leveraging spatial characteristics, to automate the classification of offshore energy infrastructure. Finally, the topside area of the oil/gas platform and the diameter length of the wind turbine are measured. This proposed framework is validated against a ground truth data set of the whole Scottish waters, covering an area of 371, 195 km^2. The major contributions of this paper can be summarized as

follows.

1) We present the first attempt to fuse the Sentinel-1 and Sentinel-2 data for geolocating of offshore energy infrastructures. By harnessing the complementary strengths of the SAR and MSI data, our approach achieves efficient and accurate geolocation of offshore energy infrastructures, including the identification of diverse rigs within interconnected oil/gas platforms, which are typically treated as a single entity in most existing studies. This work increases the necessary granularity in geolocation analysis for oil/gas platforms.

2) It is also the first time for the automated size measurement of offshore energy infrastructure from the satellite data. The diameter length of the wind turbines and the topside area size of the oil/gas platforms and semi-permanent objects are measured independently. The proposed automatic geolocation and size measurement provides a comprehensive understanding of the offshore energy infrastructure landscape.

3) A novel classification method is presented to effectively distinguish the wind turbines from other types of offshore energy infrastructure. The proposed method offers an automated pathway for the subsequent monitoring and measurement of offshore energy infrastructures, providing a streamlined approach to these crucial tasks.

II. STUDY AREAS AND DATASETS

A. Study areas

The study area covers between the Scotland's Exclusive Economic Zone and the baseline of the United Kingdom (UK) as well as the closing bays (as shown in Fig.1). Note that the infrastructure within internal waters is excluded due to the practice of 'parking' oil and gas platforms within internal waters for variable periods, and the corresponding challenge of generating accurate ground-truth data. Most infrastructure is located beyond the baseline and future energy structures are likely to be constructed further offshore [30]. Scotland is located in northwest Europe and surrounded by the North Sea on the east, the North Channel and the Irish Sea on the southwest and the Atlantic Ocean on the north and west. The water depths of the study area vary from shallow coastal waters to more than 2,000 m in some ocean areas. Scottish waters cover approximately 371,915 km^2 and contain some of the largest oil reserves in Europe. Offshore hydrocarbon exploitation begins in the 1970's and remains a major, but declining activity in Scottish waters. Typical oil and gas installations within Scottish waters include platforms that are either concrete gravity based or fixed steel jackets. Fixed steel jackets can comprise a single integrated platform or bridge-linked two or more platforms, which inevitably increases the difficulty of platform identification in satellite imagery. In recent years, the Scottish government has promoted offshore renewable energy. Several Offshore Wind farms have been constructed including Beatrice Offshore Wind farm, Moray East Offshore Wind farm (under construction), HyWind Offshore Wind farm (Aberdeenshire), Kincardine Offshore Wind farm (Aberdeenshire) and Aberdeen Offshore Wind farm (Aberdeen Bay). The

Beatrice offshore wind farm with wind turbines located 25km from the Scottish shoreline was the world's deepest offshore wind project at the time of construction. The Scottish waters also host various semi-permanent objects, i.e., the structures or installations that are intended to remain in place for an extended period of time, but are not permanent fixtures. These objects serve specific purposes and can be moved or relocated as needed. Examples of semi-permanent objects include floating production storage and offloading (FPSO) vessels, and floating storage units (FSU).

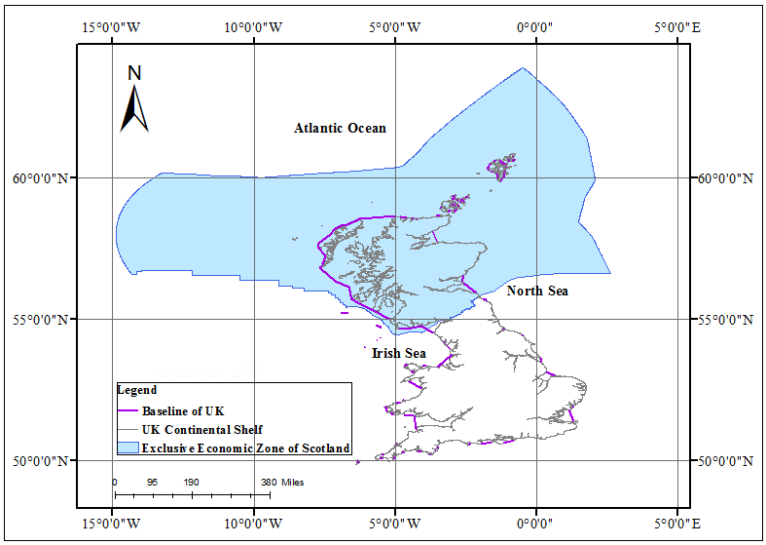

Fig. 1. The Scottish Exclusive Economic Zone: location of the study area in the North Sea.

B. Datasets

The data used in this study includes images and auxiliary data. Image data is employed to identify offshore energy infrastructure in Scottish waters and analyze their sizes. Auxiliary data is used to assemble the ground truth dataset and validate the spatial distribution and size of offshore infrastructure, and performance evaluation.

1). Ground truth dataset

In this paper, a ground truth dataset of offshore energy infrastructures is constructed using: (1) Scottish Waters (200M Limit) - Exclusive Economic Zone (EEZ) [30], (2) The Scotland coastline and baseline [31], (3) The Oslo and Paris Commissions (OSPAR) Inventory of Offshore Installations-2019 [32], (4) The offshore infrastructure distributions on the UK's Continental Shelf provided by the Oil and Gas Authority (OGA) [33], (5) The actual topside area size of oil/gas platforms measured by experts' knowledge and measurement tools which are available in the EO Browser interface [34], (6) The Beatrice Offshore Wind Farm Consent Plan [35], (7) Development Layout and Specification Plan for Moray East Offshore Wind Farm [36], (8) The Design Statement for Aberdeen Offshore Wind Farm [37], (9) The Construction Plan for Hywind Wind Farm [38], and (10)

Kincardine Offshore Wind Farm Environmental Scoping Assessment [39]. The summarized ground truth data is given in Tables S1-S6 of the Supplementary.

2). Images for the proposed method

The satellite data used in this study includes the Sentinel-1 SAR data and Sentinel-2 MSI data.

Sentinel-1, developed by the European Space Agency (ESA) as part of the Copernicus program, is a constellation of two radar imaging satellites: Sentinel-1A and Sentinel-1B. Launched on April 3, 2014, and April 25, 2016, respectively, these satellites are equipped with a SAR instrument, which operates in the C-band frequency range, enabling the measurement of the backscatter signals reflected from the Earth's surface. The repeat cycle for a single Sentinel-1 satellite is 12 days, while combined operation of the Sentinel-1A and Sentinel-1B satellites used to ensure a revisit cycle of 6 days [40], [41]. SAR images acquired by the Sentinel-1 encapsulate both coherent, signifying interferometric phases, and incoherent, pertaining to the amplitude features, components of information. Sentinel-1 offers several imaging modes to cater to diverse user needs. These include the Stripmap (SM), Interferometric Wide Swath (IW), Extra Wide Swath (EW), and Wave (WV) modes. The Interferometric Wide Swath (IW) mode is particularly valuable for large-scale monitoring and mapping activities. It captures the SAR images with a swath width of up to 250 kilometers and achieves a spatial resolution of 5×20 meters. Additionally, the IW mode provides valuable dual-polarization data, including the vertical transmit and vertical receive (VV) and the vertical transmit and horizontal receive (VH) polarization. The orthorectified VH Sentinel-1 data can be achieved using preprocessing steps including the radiometric calibration, thermal noise removal, speckle filter, geometric correction, orthorectification and terrain correction.

The Sentinel-2 data were also acquired from the ESA, which operate as part of the Copernicus program. The Sentinel2A (launched on June 23, 2015) and 2B (launched on March 7, 2017) satellites offer a combined revisit period of 5 days and possess a wide swath width of 290 kilometers. Both Sentinel-2A and Sentinel-2B satellites are equipped with a single multispectral instrument that captures imagery across 13 spectral bands. These bands include visible (VIS), near-infrared (NIR), and short-wave infrared (SWIR) bands with a spatial resolution of 10m, 20m and 60m, respectively. The Sentinel-2 data can be processed to obtain higher-level surface reflectance products (Level-2A) by transforming the top-of-atmosphere (TOA) reflectance product (Level-1C) using atmospheric correction techniques. In this study, the bands in blue (Band #2), green (Band #3) and red (Band #4) of Sentinel-2 Level-2A data are used.

The main advantage of the Sentinel-1 data lies in its ability to provide all-weather and day-and-night imaging capabilities through the use of SAR technology, overcoming the limitations of cloud cover in Sentinel-2 level 2A data. On the other hand, Sentinel-2 level 2A data, with its optical imaging capabilities, offers higher spatial resolution and richer spectral information. This facilitates the observation of intricate details on the Earth's surface, like small sized infrastructure and complex oil/gas structures.

In this paper, we selectively downloaded 95 orthorectified VH Sentinel-1 images, covering the period from June 2020 to February 2022 and 33 Sentinel-2 Level 2A data with RGB bands spanning from March 2020 to February 2022 from the EO browser [34]. The software and metadata used to generate the results in this paper are provided by DOI of 10.5281/zenodo.8171739.

III. METHODOLOGY

The proposed method includes two schemes: location detection and size estimation. Figure 2 shows the workflow of the framework. First, the Sentinel-1 time-series data are processed through three strategies to detect the 'guided area', or estimated contour position of the candidate offshore infrastructures. Then, this 'guided area' is used to quickly locate the offshore candidates in locally cloud free Sentinel-2 data. Finally, three steps are employed based on clear shape and structural information on Sentinel-2 to refine the location and estimate the size of each structure.

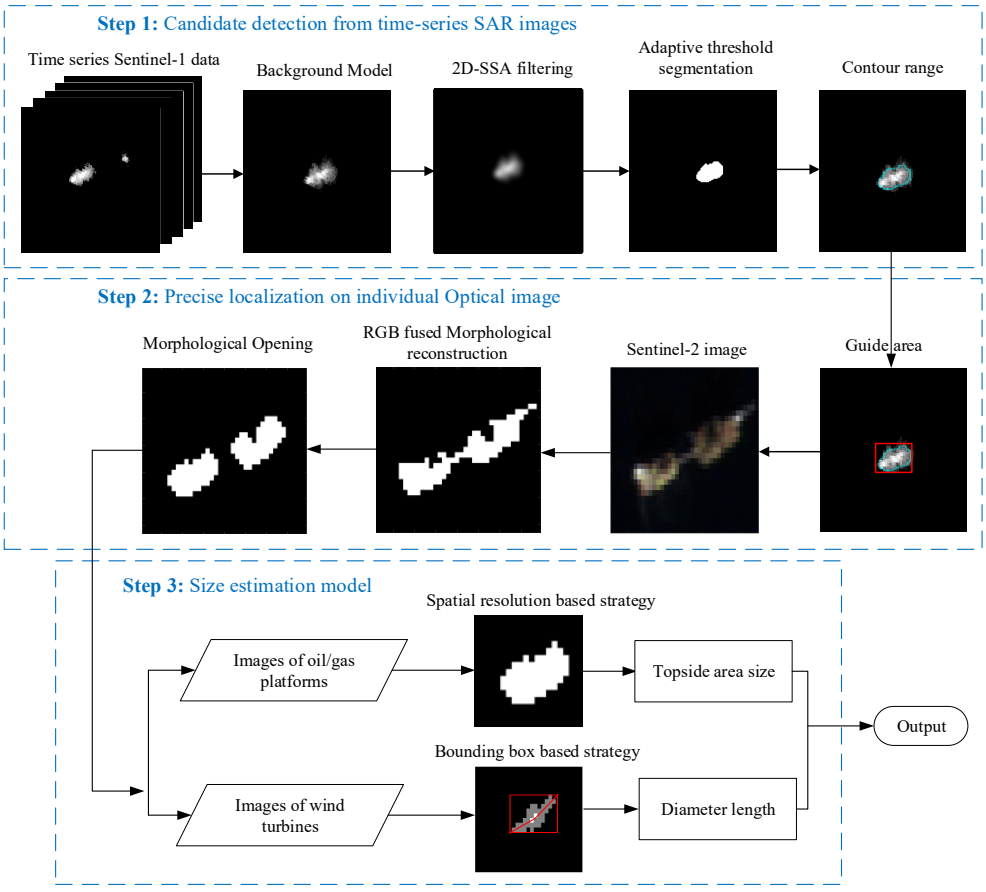

Fig. 2. The flowchart of the proposed method.

Data fusion model for Geolocation of interested objects

1). Candidate detection from Sentinel-1 time-series data

(a) Temporal analysis for modeling of background targets

The ocean surface is a dynamic environment. There are a variety of moving objects and changing wakes generated in the surrounding water of offshore infrastructure. However, oil/gas platforms and wind turbines have a temporally invariant position. For detecting these offshore infrastructures, it is essential to design an effective background model by removing the moving, short-duration, or subtly shifting objects. In general, the running average and mixed Gaussian model are widely used for modelling the background [7], [15]. However, the running average method is easily affected by the noises in monophase image. The Gaussian model requires high computational cost. In this paper, a simple and fast method, namely temporal median filtered approach [27] is applied.

The SAR time series data is adopted to model background targets by using temporal changes. For each scene, the Sentinel-1 time-series images are employed. The median intensity value of each pixel from time-series images is calculated as follows:

$$I^M(x,y) = \text{median}\{I_n(x,y)\} \quad n = 1, 2, \dots, N \tag{1}$$

where (x, y) is the pixel location, I_n is the n-th image in the time-series, N denotes the total number of time-series images, and I^M is the median image, i.e., the estimated static background. To balance between the detection accuracy and computational efficiency, N is set to 5 in this study. Among time-series images, the oil/gas platforms and wind turbines have a higher occurrence frequency than the moving objects. As a result, on the temporal median filtered image, due to low occurrence frequency, the vessels and speckle noises can be successfully removed.

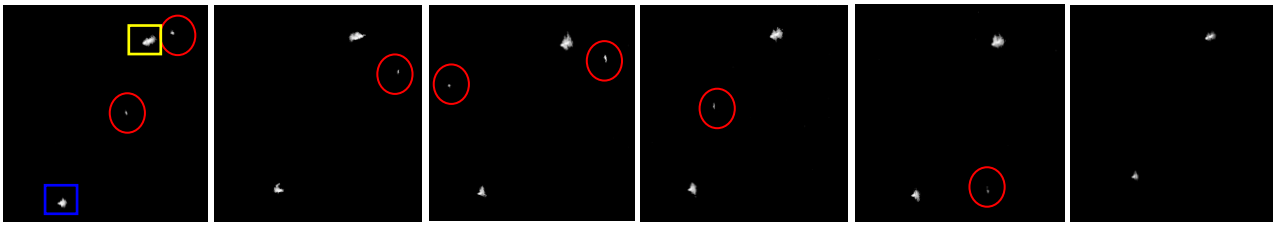

(a) (b) (c) (d) (e) (f)

Fig. 3. The platform Clair (marked in blue rectangle), and the linked platform consisting of Clair Ridge Drilling and Process (DP) and Clair Ridge quarters and utilities (QU) (marked in yellow rectangle), and false positives (vessels and noise, marked in red circles) in the Sentinel-1 data: (a) data ID: 2020-06-20-00_00_2020-06-20-23_59_Sentinel-1_AWS-IW-VVVH_VH_-_decibel_gamma0_-_orthorectified; (b) data ID: 2020-08-19-00_00_2020-08-19-23_59_Sentinel-1_AWS-IW-VVVH_VH_-_decibel_gamma0_-_orthorectified; (c) data ID: 2020-10-18-00_00_2020-10-18-23_59_Sentinel-1_AWS-IW-VVVH_VH_-_decibel_gamma0_-_orthorectified; (d) data ID: 2020-12-17-00_00_2020-12-17-23_59_Sentinel-1_AWS-IW-VVVH_VH_-_decibel_gamma0_-_orthorectified; (e) data ID: 2021-02-15-00_00_2021-02-15-23_59_Sentinel-1_AWS-IW-VVVH_VH_-_decibel_gamma0_-_orthorectified; (f) the temporal median image of five time-series images.

As shown in Figs. 3 (a-e), different vessels (marked in red circles) appear on the Sentinel-1 data at different dates, whilst there are ships close to the oil/gas platforms. This will inevitably increase the difficulty to remove them from the images. Using the subtle position changes, the temporal median operation has successfully filtered these ships and reduced the noise as depicted in Fig. 3(f). Overall, the background ocean noise is suppressed yet the offshore infrastructure is accentuated. Similar results are also obtained for the wind farm areas. It is clear from Figs. 4 (a-e) that, as expected, the blade part of wind turbine changes direction over time. By considering the wind turbine at different dates via the temporal median operation, the main structures of these rotating objects are maintained with the background noise removed.

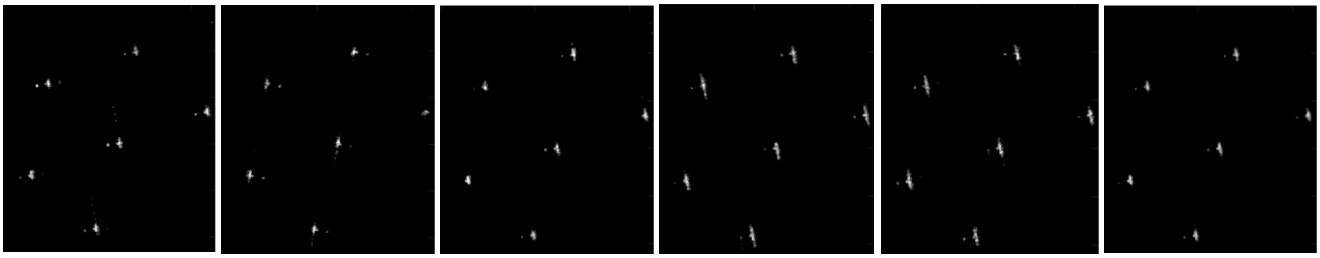

(a) (b) (c) (d) (e) (f)

Fig. 4. Five Sentinel-1 SAR images of the offshore wind turbines in the Beatrice wind farm: (a) data ID: 2020-06-20-00_00_2020-06-20-23_59_Sentinel-1_AWS-IW-VVVH_VH_-_decibel_gamma0_-_orthorectified; (b) data ID: 2020-08-19-00_00_2020-08-19-23_59_Sentinel-1_AWS-IW-VVVH_VH_-_decibel_gamma0_-_orthorectified; (c) data ID: 2020-10-18-00_00_2020-10-18-23_59_Sentinel-1_AWS-IW-VVVH_VH_-_decibel_gamma0_-_orthorectified; (d) data ID: 2020-12-17-00_00_2020-12-17-23_59_Sentinel-1_AWS-IW-VVVH_VH_-_decibel_gamma0_-_orthorectified; (e) data ID: 2021-02-15-00_00_2021-02-15-23_59_Sentinel-1_AWS-IW-VVVH_VH_-_decibel_gamma0_-_orthorectified; (f) The result of temporal median image.

(b) 2D-SSA Filtering for smoothing the images

The temporal median operation can minimize the noisy objects of moving objects in the background. However, there is still other noise remained, especially the water wake around the offshore infrastructure, which can affect the geolocation accuracy [42]. In order to filter such noise on the edges of infrastructure while keeping more details and clear contours, the 2D-SSA method is employed, which is an effective and noise-robust spatial feature extraction tool [43]. For a grayscale image, the 2D-SSA method can decompose the image into several components and reconstruct a new image with the main information and spatial structures. For the image I^M with size of $N_x \times N_y$, a sliding window L with size of $L_x \times L_y$, where $L_x \in [1, N_x]$ and $L_y \in [1, N_y]$ is defined. Then, a trajectory matrix $X \in R^{L \times K}$ can be generated, where $K = (N_x - L_x + 1)(N_y - L_y + 1)$. The matrix X exhibits a structure called the Hankel-block-Hankel (HbH), which is Hankel in block terms with each one of the blocks being Hankel by itself [43]. The matrix X is decomposed by the singular value decomposition (SVD), resulting in eigenvalues and corresponding eigenvectors. Afterwards, the eigenvalue grouping (EVG) is carried out, wherein multiple components are chosen to form a new matrix X_t through grouping. Note that the resulting matrix X_t is not necessarily HbH type. In order to transform X_t

into HbH matrices, a two-step Hankelization operation is used, which involves first applying an averaging procedure within each block and subsequently applying it between the blocks. Finally, the reconstructed final image I^{Re} is obtained. Details description of the 2D-SSA process can be found in [43]. In this paper, the number of components N_c and the size of the filtering window in 2D-SSA is set to 1 and 5×5, respectively. The determination of these parameters is illustrated in Figs. S1-S2 of the Supplementary.

(c) Adaptive Threshold Segmentation for object detection

After obtaining a filtered image, an adaptive threshold segmentation is applied to extract the candidate regions of interests as potential objects. The widely used method, OTSU [44] is employed here to adaptively determine an optimal threshold for each scene by maximizing the weighted sum of between-class variance of the foreground and the background. Specifically, OTSU is first applied to obtain the threshold value T_{S1}. Pixels with intensity values higher than T_{S1} are considered as for offshore infrastructure as below:

$$OD_{s1}(x,y) = \begin{cases} 1, & \text{if } I^{Re} > T_{S1} \\ 0, & \text{otherwise} \end{cases} \tag{2}$$

As seen in Figs. 5 (a) and 5(f), there is lots of noise remaining in the temporal median image, especially on the edges of the object. We can find from Figs. 5 (c) and 5(h), the 2D-SSA filter can effectively smooth the temporal median image especially on the edge area. When applying the threshold segmentation, the detection results in Figs.5 (b) and (g) show many noises at the edges, even on the ocean background (marked with red circle). In contrast, the segmentation on 2D-SSA filtered image as shown in Figs. 5 (d) and (i) presents better performance. Based on the detection result in Figs. 5 (d) and (i), the contour range can be acquired as shown in Figs. 5 (e) and (j). From Fig. 5, for different kinds of offshore infrastructures with varying characteristics, the OTSU method exhibits effective performance in selecting a proper threshold to extract the contour ranges. However, due to the low spatial resolution, it is difficult to detect the location of each platform from the linked platform's structure as shown in Figs. 5 (a)-(e). That is, the linked platforms are identified as one object. This problem will be further addressed by combining Sentinel-1 with the high-resolution Sentinel-2 data in the next subsection.

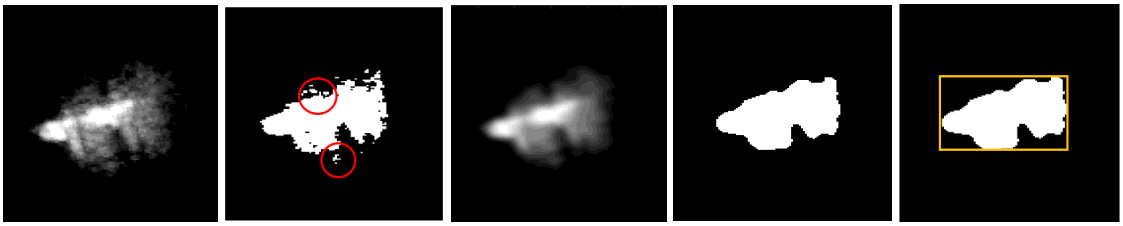

(a) (b) (c) (d) (e)

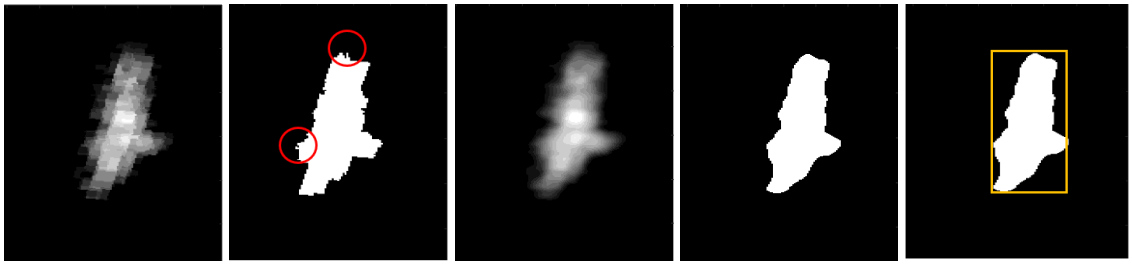

(f) (g) (h) (i) (j)

Fig. 5. The 2D-SSA filtering and threshold segmentation results: (a) The temporal median image of the linked platforms Clair Ridge DP and Clair Ridge QU; (b) Threshold segmentation results on (a); (c) The 2D-SSA filtered image of (a); (d) Threshold segmentation results on (c); (e) The detected contour range on (d); (f) The temporal median image of the wind turbine BE-A5; (g) Threshold segmentation results on (f); (h) The 2D-SSA filtered image of (f); (i) Threshold segmentation results on (h); (j) The detected contour range on (i).

2). Precise localization on individual Sentinel-2 data

Without the effect of clouds, the Sentinel-1 data can efficiently obtain the approximate locations of offshore infrastructure. Then, the high-resolution Sentinel-2 data is further applied for precise localization. As shown in Figs. 6 (a-b), the detected object from Sentinel-1 has indicated a larger size than that from the Sentinel-2 image, due mainly to the wake detected around the oil/gas platforms in the Sentinel-1 data. The SAR sensor in Sentinel-1 is particularly sensitive to the surface roughness and can capture the wakes created by moving vessels or oil/gas platforms on the water [45]. In contract, Sentinel-2 is equipped with a multispectral optical sensor and focuses on the land monitoring [46]. The wakes are invisible or non-distinguishable in Sentinel-2 images, as shown in Fig. 6 (b). Given this, the detected contour range on Sentinel-1 data in Section III.A.1) is taken as a 'guided area' to refine the precise detection of the offshore infrastructures using the Sentinel-2 data, especially for the separation of the linked structures. In this section, a spectral-spatial detection method, namely RGB fused morphological reconstruction is proposed.

The morphological reconstruction can extract spatial features by fully utilizing the shape and size information of objects from the input image. Given the different distinguishability of red, green and blue bands in Sentinel-2 image, the morphological reconstruction is separately performed on the R, G and B channels. First, the opening-by-reconstruct operation is applied as follows:

$$O_R = \bigvee_{k\geq 1} D_{I_R}^{(k)}(I_R \ominus b) \tag{3}$$

where I_R is the R channel in Sentinel-2, b is the structural element and $(I_R \ominus b)$ is the erosion of I_R by b. Here a disc structural element is employed because it satisfies the rotation invariance thus can avoid causing potential distortion of image features [47]. The radius size of b is set to 2. The grayscale reconstruction $D_{I_R}(I_R \ominus b)$ is operated by iterating grayscale geodesic dilations for k times until stability is reached. In each iteration, it is calculated as below:

$$D_{I_R}^{(1)}(I_R \ominus b) = [(I_R \ominus b) \oplus b] \wedge I_R \tag{4}$$

where $\oplus$ stands for the dilation and $\wedge$ presents the pointwise minimum.

Then, a closing-by-reconstruction is used to refine the shape.

316 $$C_R = \bigvee_{k\geq 1} E_{O_R}^{(k)}(O_R \oplus b) \tag{5}$$

317 $$E_{O_R}^{(1)}(O_R \oplus b) = [(O_R \oplus b) \ominus b] \vee O_R \tag{6}$$

where $\vee$ stands for the pointwise maximum.

In morphological reconstruction, the erosion and dilation can significantly remove irregular noises on object surface, while the pointwise computation with input image maintains the shape details of objects. Finally, a threshold also using OTSU is obtained, T_{S2}, to extract the object pixels. As a consequence, the final result OD_f is obtained by using decision fusion of the detection results in three channels, OD_R, OD_G and OD_B, as below:

$$OD_f = OD_R \odot OD_G \odot OD_B \tag{7}$$

where $\odot$ stands for the Hadamard product. That is, only the pixels detected by all channels are regarded as objects.

Postprocessing using an adaptive morphological opening operator is then applied on OD_f to remove noise and bridges in linked platform. In this operator, the erosion operation can remove bridges and followed dilation operation can re-add the pixels on edges guaranteeing accurate evaluation of area size of offshore infrastructure. In morphological opening operator, an adaptive structural element is proposed.

$$d_i = \left\lfloor \left(\frac{La_i - L_{gmin}}{L_{gmax} - L_{gmin}} \times (w_2 - w_1 + 1) + w_1 \right) \times \frac{r_{s2}}{r_i} \right\rfloor \tag{8}$$

where r_{s2} presents the spatial resolution of Sentinel-2 image, i.e., 10 meters. The L_{gmax} and L_{gmin} are the maximum and minimum length of major axis in the obtained 'guided area' of all detected objects. For the *i*-th detected object, d_i is the radius value, r_i is the spatial resolution of the input image and La_i stands for the length value of major axis of its 'guided area'. The $[w_1, w_2]$ denotes the range of d_i, and set to [0, 1] in this paper. In this way, the morphological opening is only operated on the linked platforms with large 'guided area' size. This setting avoids the loss of blades in the detection of wind turbines.

From Figs. 6, it is clear that the linked platforms can be effectively extracted. The RGB fused morphological reconstruction method maintains the shape of the offshore infrastructure. As shown in Fig.6 (e), the adaptive postprocessing strategy successfully remove the bridges in linked platforms.

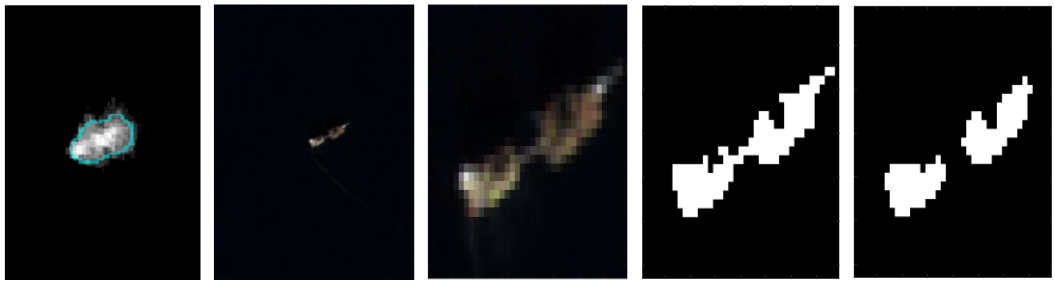

(a) (b) (c) (d) (e)

Fig. 6. The platform identification from the linked structure of Clair Ridge DP and Clair Ridge QU. (a) The linked structure in Sentinel-1 data with the contour range marked in cyan, (b) The linked structure in Sentinel-2 true color image covered the same latitude and longitude range of (a), (c) The zoomed in image of (b) in 'guided area' (contour range), (d) The detection result OD_f using RGB fused Morphological Reconstruction, (f) The detection result after adaptive morphological opening operator.

B. Size estimation model

In this section, based on the geolocation results, the topside area of oil/gas platforms and the diameter of wind turbine, is further determined for evaluation, as detailed below.

(a) Offshore infrastructure classification

First, wind turbines need to be separated from the oil/gas platforms and other targets, before applying different kinds of measurement. To achieve this, here two parameters, the minor axis and the circularity of the 'guided area' are utilized.

$$\text{circularity} = \frac{4\pi \times Np}{P^2} \tag{9}$$

where Np is the number of pixels in one detected object on Sentinel-2 data and P stands for the perimeter value. Wind turbine usually present smaller topside area than almost all other kinds of offshore infrastructures. However, there are some small-sized infrastructures, such as the rig Mungo and Beryl Single Point Mooring (SPM)-3. Because of the long and slender blades, the wind turbines present a low circularity, whereas some semi-permanent objects, such as the floating production storage and offloading (FPSO) also have low circularity. Therefore, in order to well separate the wind turbine from all oil/gas platforms and semi-permanent objects, the Eq. (10) is adopted. That is, for the i-th detected object, if its minor axis of 'guided area' smaller than or equal to 10 and the circularity value smaller than 1, it is classified as wind turbine.

$$f(i) = \begin{cases} 1, & \text{if } Lo_i \leq 10 \; and \; \text{circularity} < 1 \\ 0, & \text{otherwise} \end{cases} \tag{10}$$

where Lo_i stands for the length value of minor axis of its 'guided area'.

(b) Determining the topside area of oil/gas platforms

In the Sentinel-2 images, the topside area of the oil/gas platform, defined as the platform area above the sea level, can be calculated based on the spatial resolution of the images. Given a spatial resolution of r_{S2} (meter), the topside area of one

identified platform in the Sentinel-2 image is defined as follows:

$$S = Np \times r_{S2}^2 \tag{11}$$

where S donates the topside area of one oil/gas platform.

(c) Estimating the diameter of wind turbines

The structures of slender blades and nacelle of the wind turbine can be observed in Sentinel-2 image (Fig.7). As shown, the diameter can be calculated as twice the length of one blade. As shown in Fig.7 (a), θ is the rotational azimuth of one blade. When θ equals to 90°, the full length of one blade is presented. Then, a bounding-box based strategy is used to locate two blades of one wind turbine in Sentinel-2 image.

(a) (b) (c) (d)

Fig. 7. The diameter length evaluation of wind turbines: (a) Wind turbines diagram; (b)The true color Sentinel-2 image of three wind turbines in the Aberdeen offshore wind farm; (c) A zoomed-in view of a single wind turbine with blade highlighted with yellow rectangular and nacelle marked with red circle. (d) The detected wind turbine structure and bounding box settings.

A morphological erosion operation with a disc structural element, a radius of 1, is employed to erode the slender blades before detecting the center of nacelle parts. As shown in Fig.7 (d), the detected whole wind turbine is highlighted in grey, and the pixels of the nacelle center parts detected by the erosion operation are marked in white. By using the locations of nacelle pixels and the bounding box, the diameter of the wind turbine, *Dist*, is calculated as twice the length of the longer blade.

$$Dist = 2 \times \max\left(\sqrt{(x_{nac} - x_1)^2 + (y_{nac} - y_1)^2},\ \sqrt{(x_{nac} - x_2)^2 + (y_{nac} - y_2)^2}\right) \tag{12}$$

where (x_{nac}, y_{nac}) is the center location of nacelle pixels; (x_1, y_1) and (x_2, y_2) denote locations of top of two blades.

However, in most cases, the angular $\theta \neq 90°$. Consequently, only portions of the wind turbine blade are captured in the Sentinel-2 images as it keeps rotating. To improve the measurement accuracy, 12 consecutive images from a Sentinel-2 time-series images are utilized. Specifically, the diameter is first calculated in each image, with the maximum in every 4 images is selected. The final diameter of one wind turbine is determined by averaging three maximum values.

C. Validation

A mask generated using the Scottish Exclusive Economic Zone (EEZ), the Scotland coastline and baseline is utilized to

exclude the land and islands areas. The performance of the proposed method is quantitatively assessed in terms of the accuracy of the geolocation and size measurement of the offshore infrastructures within the whole study area. The ground truth constructed in section II.B, including the latitude, longitude and size for each offshore infrastructure, is given in Tables S1-S6 of the Supplementary.

For quantitative evaluation of the geolocation of the offshore energy infrastructures, the detection probability, overall accuracy, commission rate and omission rate are employed. As illustrated in Fig. S3 of the Supplementary, the ground truth only provides an approximate location of the target infrastructure, which is not situated at the exact center of the target. Therefore, the proposed method extracts all pixels that belong to each detected infrastructure to form a location range as the detection outcome. If the detected location range contains the positioned ground truth point, it is considered as a correct detection. Otherwise, if a detected location range does not encompass any positioned ground truth point, it can be deemed as a commission error, i.e., false detection. This occurrence arises due to the misidentification of other objects as offshore energy infrastructure. In the case that no location range is detected for a positioned ground truth point, it is regarded as an omission by the proposed method.

The detection probability *DP*, overall accuracy *OA*, commission rate *CR* and omission rate *OR* are calculated as follows, where *Na, NG, Nc* and *No* denote respectively the number of offshore energy infrastructure that are correctly detected, the actual total number of offshore energy infrastructure in the ground truth data, the number of the objects that are misidentified as the offshore energy infrastructure, and the number of offshore energy infrastructure that are omitted by the proposed method.

$$DP=Na/(NG\times 100\%) \tag{13}$$

$$CR=Nc/(NG\times 100\%) \tag{14}$$

$$OR=No/(NG\times 100\%) \tag{15}$$

$$OA=Na/((Na+Nc+No)\times 100\%) \tag{16}$$

The comparison analysis was conducted and benchmarked with two state-of-the-art offshore energy infrastructure detection methods. The first is the Google Earth Engine offshore infrastructure detector (GEEOID), using the Sentinel-1 SAR data [6]. GEEOID used the median-filtered composite strategy, difference of Gaussians and postprocessing operations of erosion and dilation. The offshore infrastructure map capability of GEEOID has been validated through the detection of the oil platforms in the Gulf of Mexico and extraction of the wind turbines in the waters of China and the United Kingdom. In this study, the prior testing of parameter settings is carried out in the Scottish waters. The optimal configurations encompassed the 50 meters in erosion, 5 meters in dilation, and a threshold value set at 0.85. For analysis, the Sentinel-1 data from June 2020 to January 2022 are adopted. The second compared method is the NDWI composite method [15] based on the optical imagery, includes the minimum NDWI (Min_NDWI), maximum NDWI (Max_NDWI) and mean NDWI (Mean_NDWI). It uses the Landsat-7 ETM+ images in two consecutive years in the Caspian Sea for identification, and Night-light data and Sentinel-2 images for verification.

Different thresholds are applied on the NDWI composite to classify the water, island and offshore oil/gas platforms with certain rules: water body (Max_NDWI>0.55), island (Min_NDWI<-0.05) and offshore oil/gas platforms (0<Mean_NDWI<0.4). Herein, we apply the NDWI composite method to the Scottish waters to investigate its performance. To ensure comprehensive coverage of the entire study area in the Scottish waters, this study utilizes data from Landsat 7, Landsat 8, and Sentinel-2 in two consecutive years, i.e., from June 2020 to July 2022. The optimal threshold value for oil/gas platform extraction is set to 0.3 after trail tests in the study area.

For evaluating the size detection accuracy, the size error (SE) and mean size error (MSE) are utilized. Here SE indicates the difference between the extracted size and the actual size of each infrastructure in the ground truth, and MSE denotes the average SE value for all the extracted offshore infrastructures. Considering the varying sizes of different offshore infrastructures, the size error rate (SER) is also computed as the ratio of SE and the actual size of each offshore energy infrastructure, as well as the mean size error rate (MSER) which refers to the average SER for all the detected infrastructures.

The proposed method is implemented using the Matlab 2018a platform on a computer with an Intel (R) Core (TM) i7-8700 CPU (3.20 GHz) and 16.0 GB of memory.

IV. RESULTS

A. Geolocation accuracy analysis

1). Quantitative evaluation of the geolocation accuracy

In Scottish waters, a diverse range of offshore energy infrastructure can be found, including oil/gas platforms, semi-permanent objects, and wind turbines. Table I provides a summary of their respective quantities. By combining the Sentinel-1 SAR data and Sentinel-2 MSI data, our method can correctly detect 332 objects only with one omission. The one omission is from the bridge-linked platforms, i.e., BERYL FLARE. Thus, for all offshore infrastructure in Scottish waters, the probability of detection and overall accuracy is 99.70 % and the commission error rate is 0%. Specifically, the detection probability is 100% for offshore wind turbines, single oil/gas platforms and semi-permanent objects. The detection probability for bridge-linked platforms is 97.92%. More discussions are given in Section V. Fig. 8 illustrates the spatial distribution of the detection results, while the detected location range is detailed in Tables S7-S12 of the Supplementary document.

As shown in Fig.8, the correctly identified offshore infrastructures are marked as red dots and omissions are highlighted as yellow dots. The zoomed in images for area A show the detection in the east part of the EEZ, from which we can find the distribution of the omitted structure. The zoomed in image for area B presents the wind turbines distribution in the Beatrice offshore wind farm and Moray East offshore wind farm. As seen in Fig. 8, most offshore infrastructures are located in the eastern waters of Scotland. This intensive distribution results in more background noise and moving vessels.

TABLE I

THE NUMBER OF DIFFERENT OFFSHORE INFRASTRUCTURE IN THE GROUND TRUTH.

Offshore Infrastructure	Categories	Number
Oil/gas Platform	Single	54
	Bridge-linked	48
Wind Farm	Beatrice	86 wind turbines and 2 offshore transformer modules (OTMs)
	Moray East	100 wind turbines and 3 offshore substation platforms (OSP)
	HyWind	5 wind turbines
	Kincardine	5 wind turbines
	Aberdeen	11 wind turbines
Semi-permanent objects	-	19

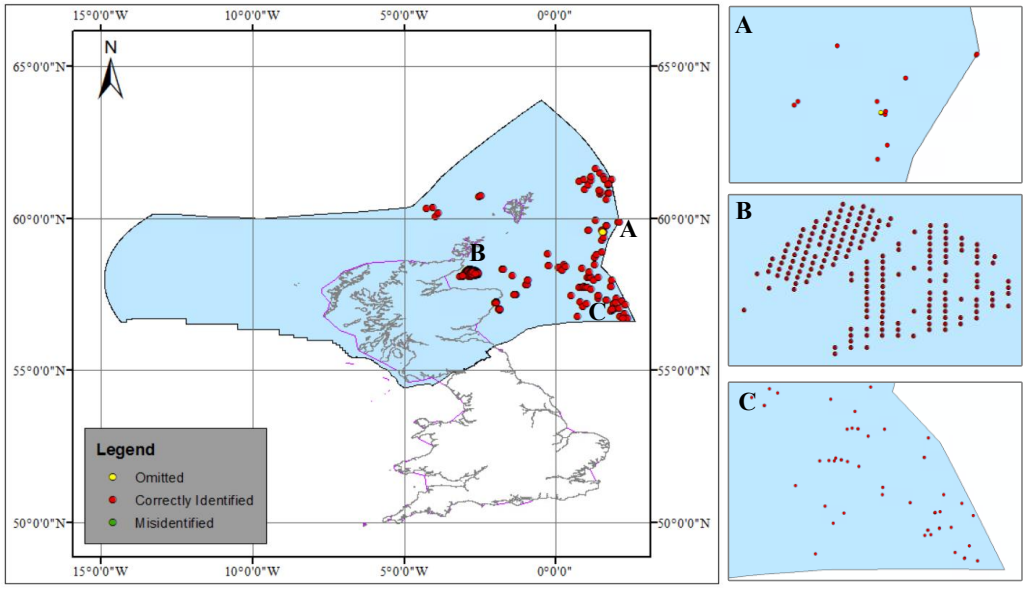

Fig. 8. Offshore infrastructure detection results by our proposed method.

2). Comparison with other methods

The comparison results are given in Table II. With an overall accuracy of 95.86%, the GEEOID method can successfully detect 324 out of 333 offshore infrastructures in Scottish waters. Specifically, all the wind turbines are successfully identified with a detection probability of 100%. In comparison to the proposed method, GEEOID generates several omissions that primarily arise from linked oil/gas platforms with intricate structures. The original literature of GEEOID [6] states that these linked oil/gas platforms are considered as a single infrastructure, without attempting to differentiate the individual rigs within each linked oil/gas platform. Consequently, the coarse resolution of Sentinel-1 data utilized by GEEOID fails to provide

sufficient detailed information for accurate identification and differentiation.

TABLE II

THE DETECTION RESULTS OF DIFFERENT METHODS ON 333 OFFSHORE INFRASTRUCTURES IN SCOTTISH WATERS

Metrics	The proposed method	GEEOID	NDWI composite
Correct Identification	332	324	300
Commission	0	5	11
Omission	1	9	33
Commission rate	0%	1.50%	3.20%
Omission rate	0.30%	2.70%	9.90%
Overall accuracy	99.70%	95.86%	87.20%

As seen in Table II, the NDWI composite method generates an overall detection accuracy of 87.20%. Compared with other two methods, the NDWI composite produce more omissions, which mainly from the wind farm areas and linked oil/gas platforms. The offshore infrastructure detection in Scottish waters is more complicated due to that there are different kinds of infrastructures including oil/gas platforms, wind turbines, semi-permanent objects and so on. The frequent cloud coverage on optical data and the fixed threshold value settings have led to the difficulties in detecting small sized wind turbines. Although clouds and shadow removal algorithms are employed to reduce the influence on NDWI index, many noise objects are still remained and result in the misidentifications.

B. Evaluation of the estimated size accuracy

1). Size accuracy of the topside of oil/gas platform and semi-permanent objects

The calculated topside area of all correctly identified oil/gas platforms and semi-permanent infrastructure are listed in Table S13 of the Supplementary, where the size evaluation accuracies are summarized in Table III and Table IV for comparison. With a spatial resolution of 10 meters, the area size of the corresponding surface for one pixel is 100 square meters (m^2). As shown in these tables, our proposed strategies for evaluating the topside area achieve promising results. For the 19 semi-permanent objects and 101 oil/gas platforms detected by our method, there are 12 rigs, i.e., Ninian north, Northern Producer, Brent Bravo, Brent Delta, Beatrice Charlie, Betrice Alpha Drilling, Beatrice Alpha Production, Beatrice Bravo, Manifold and Compression Platform 01 (MCP01), Frigg Treatment platform 1 (TP1), Frigg Concrete drilling platform 1 and Frigg Treatment Compression Platform 2 (TCP 2), have undergone decommissioning in recent years with many structures being removed or partially removed. For these decommissioning structures, accurate detection of cut legs above the water is of minor importance in documenting offshore energy infrastructure, as this is a temporary state during the decommissioning process. Final decommissioning in the North Sea

requires that all platforms are either fully removed, or cut to footing below the sea surface with no surface elements remaining. To this end, we exclude such objects in size evaluation in this paper. As a result, the topside sizes of 89 oil/gas platforms and 19 semi-permanent objects are evaluated.

TABLE III

THE CORRESPONDING NUMBER OF INFRASTRUCTURE WITH DIFFERENT SIZE ERROR AND MEAN SIZE ERROR

Categories	Oil/gas platform	Semi-permanent object
SE < 100 m^2	20	5
SE < 300 m^2	55	7
SE < 500 m^2	82	9
Total Number	89	19
MSE	45.5	765.9

As shown in Table III, for 20 out of 89 rigs (or 22.473%), the size error is lower than 100 square meters, i.e., less than one pixel in Sentinel-2 images. For 55 oil/gas platforms (or 61.80%), the SE is lower than 300 square meters, i.e., 3 pixels. On the other hand, more than 5 pixels SE is generated on seven rigs, namely Cormorant A, Eider, Piper B, Brae A, Golden Eagle Wellhead Platform, Golden Eagle PUQ Platform and Elgin PUQ. The linked platforms usually exhibit large contour range in the Sentinel-1 data, which leads to a high radius value setting of structural element in morphological opening operation. However, the rigs in linked structure usually have different topside area size. The smaller rig in the linked platforms will be recognized as a smaller size than its actual area. Overall, the MSE on the oil/gas platforms is 45.5 m^2, i.e., less than one pixel in Sentinel-2 images, which has validated the effectiveness of our proposed method. With regard to the SER given in Table IV, there are 8 infrastructures (or 8.99%) with a SER lower than 1%, while 63 structures (or 70.79%) have a SER smaller than 10%. On 7 infrastructures (or 7.87%), the SER is larger than 20%, which includes Beryl Alpha, Beryl SPM-3, Bruce D, Golden Eagle Wellhead Platform, Forties Unity, Cats Riser and Elgin PUQ. These infrastructures have relatively small topside area sizes. Thus, even they show small size error around 3 pixels in the Sentinel-2 image, the size error rates are still high and further increase the mean size error rate. On the contrary, there are infrastructure, such as Cormorant A, Piper B and Brae A, show high size errors but low size error rates. This is mainly because they have large actual topside area sizes. These results further validate the challenges of estimating the size on linked rigs. More details on the infrastructure with large SE and SER are discussed in Section V.

As for the topside area estimate of semi-permanent objects, 5 out of 19 (or 26.32%) has achieved a SE lower than one pixel in the Sentinel-2 images, while 7 out of 19 (or 36.84%) obtain an error lower than 300 square meters, or 3 pixels in the Sentinel-2

image. There are 9 objects (or 47.37%) are detected with a SE higher than 500 square meters, or 5 pixels in the Sentinel-2 image. In contrast to the oil/gas platforms with a fixed location, the semi-permanent objects would drift with waves. In the Sentinel-1 time-series images, only the parts of semi-permanent objects with high repetition are detected. Therefore, the detected contour range in the Sentinel-1 is too small to extract the whole size of these objects in the Sentinel-2 images. The obtained mean size error becomes 765.9 square meters (or around 8 pixels in the Sentinel-2 image), which is higher than that of oil/gas platforms. Similarly, these semi-permanent structures present a high MSER of 12.56% as shown in Table IV. Here, 4 objects (or 21.05%) have a SER higher than 20%, including Kraken FPSO, Alba FPSO, Pierce FPSO and Culzean FPSO. Our method only detects their partial structures due to the limited contour range. They also have a higher SE than 20 pixels in the Sentinel-2 image, which significantly increase the MSE and MSER results for semi-permanent objects. However, the other 12 (or 63.16%) semi-permanent objects all show a lower SER than 10%. That is, most semi-permanent objects can achieve promising SER results.

TABLE IV

THE NUMBER OF INFRASTRUCTURE WITH DIFFERENT SIZE ERROR RATE AND THE CORRESPONDING MEAN SIZE ERROR RATE.

Categories	Oil/gas platform	Semi-permanent object
SER < 1%	8	5
SER < 10%	63	12
SER < 20%	82	15
Total Number	89	19
MSER	7.64%	12.56%

2). Accuracy of estimated diameter of the wind turbines

The accuracy of the estimated diameters of the wind turbines is evaluated in this section. Due to a low spatial resolution of 10 meters, the calculated length which is less than one pixel is presented as ± 5 meters. Table V summarizes the evaluation results of the estimated diameters for the wind turbines, where the detailed detected results from all wind farms are given in Tables S14-S18 of the Supplementary. The actual diameters in different wind farms vary in the Scottish waters, which are listed in Table V.

In the Beatrice offshore wind farm, there are 86 wind turbines apart from the two OTMs. Among them, the size error of the estimated diameters for 22 wind turbines (or 25.58%) is less than 5 ± 5 meters (SER<3.25%). For 55 wind turbines, the errors are lower than 10 ± 5 meters (SER<6.49%). In addition, the SE of all wind turbines in the Beatrice Offshore Wind farm is lower than 20 ± 5 meters (SER<12.99%), i.e., 2 pixels in the Sentinel-2 images. Overall, the MSE of wind turbines in the Beatrice Offshore Wind farm is 9.3 ± 5 meters (MSER is 6.04%), which is around one pixel in the Sentinel-2 images. In Moray East offshore wind farm, there are 100 wind turbines and three OSPs, in which 10 out of 100 wind turbines (or 10%) has a SE lower than 5 ± 5

meters (SER<3.05%). There are 59 wind turbines (or 59%) with a SE lower than 10 ± 5 meters (SER<6.10%) and 94 wind turbines with a SE lower than 20 ± 5 meters (SER<12.20%). No wind turbine is estimated with a SE larger than 30 ± 5 meters. The MSE is around one pixel in the Sentinel-2 image. In the HyWind, Kincardine and Aberdeen offshore wind farms, all wind turbines show SE lower than 10 ± 5 meters. The MSE and MSER in the HyWind, Kincardine and Aberdeen offshore wind farms are all less than 10 meters (one pixel in the Sentinel-2 image) and 5%, respectively.

TABLE V

THE DIAMETER LENGTH EVALUATION OF WIND TURBINES IN SCOTTISH WATERS

Name (Numbers)	True Length (m)	SE≤5±5 m	SE≤10±5 m	SE≤20±5 m	SE≤30±5 m	MSE (MSER)
Beatrice (86)	154	22	55	86	86	9.3 ± 5 m (6.04%)
Moray East (100)	164	10	59	94	100	10.6±5 m (6.46%)
HyWind (5)	154	2	5	5	5	5.8 ± 5 m (3.77%)
Kincardine (5)	164	2	5	5	5	6.4 ± 5 m (3.90%)
Aberdeen (11)	150	8	11	11	11	6.4 ± 5 m (4.27%)
Summary (207)	-	44	135	201	207	7.7 ± 5 m (4.89%)

In summary, there are 207 wind turbines in the study area, in which 135 (65.21%) of them have a SE lower than 10 ± 5 meters. The 201(97.10%) of wind turbines show a SE lower than 20 ± 5 meters, i.e., two pixels in the Sentinel-2 image. The MSE and MSER for wind turbines in the whole Scottish waters are 7.7 ± 5 meters and 4.89%, respectively. For the different offshore wind farms in Scottish waters, the MSE are all less than 20 ± 5 meters and the MSER are lower than 7%. These results further validate the effectiveness of our proposed method in the size evaluation of the offshore infrastructures. It provides the potential for monitoring and analyzing the wind turbine blades in the future.

V. DISCUSSIONS

Fig. 9 shows the cases of omissions in the location detection and infrastructures with a large size error in the Sentinel-1, Fig. 9. (a-b) and the final detection results, Fig. 9. (c). For the location detection, there is one omission which is from the platform complex, i.e., linked oil/gas platforms with bridges. As shown in Fig. 9 (b), our method fails to identify the platform Beryl flare in the infrastructure #1 (marked in yellow circles). This omission is because that the platform Beryl flare shows the similar spectral and spatial features with the bridges (e.g., color, size and shape). This case is more complex. The structural element in morphological opening operation can identify the pixels and the corresponding neighborhood in the image to be processed [48]. This platform is identified as the part of bridge and then removed by the morphological opening operation. For infrastructures #2 and #3, the high size error and size error rate are generated. These are mainly because that the same radius value of structural

element in morphological operators are used for all rigs in one linked structure, even though rigs show different topside area sizes. The infrastructure #2 consists of platforms Bruce PUQ, Bruce CR and Bruce D, where the platforms Bruce CR and Bruce D are identified with higher size error rate (SER) than 10%. The platform Elgin PUQ in the infrastructure #3 is identified with size error equaling to around 9 pixels in Sentinel-2 image. It is clear from Fig. 9 (b) that in the infrastructures #2 and #3, rigs have significantly different topside area sizes. The infrastructure #4 is the Beryl Single Point Mooring (SPM) -3, which has a significant smaller size than the oil/gas platform. Due to the small size, weak intensity and 2D-SSA filter used in the proposed method, the detected contour range is limited in the Sentinel-1 data. As shown in Fig. 9 (c), based on the 'guided area' obtained from the Sentinel-1 data, only part of the structure is detected and evaluated in the Sentinel-2 image. As a result, the structure is detected with a large size error rate. In contrast to the fixed position of oil/gas platform and wind turbine, most semi-permanent objects are floating steel, which makes them easily drift with waves. After the temporal median operation, only the area with high appearance frequency of these floating objects can be detected as the contour range, which inevitably narrows the 'guided area' in the Sentinel-2 images. The detection result of infrastructure #5, namely Pierce FPSO, is illustrated in Fig. 9. By comparing Fig. 9 (a) and Fig. 9 (b), it is clear that this FPSO has shifted slightly over the time. As a result, only a small part is extracted as shown in Fig. 9 (c), which significantly increases the size error evaluation. The infrastructure #6 is the wind turbine BE-G12 in the Beatrice offshore wind farm. As shown, the proposed method fails to extract the nacelle part correctly, which leads to the error in blade length estimate and finally obtain a short diameter size. For most wind turbines, the generated size error is mainly due to the inaccurately detected location of nacelle parts.

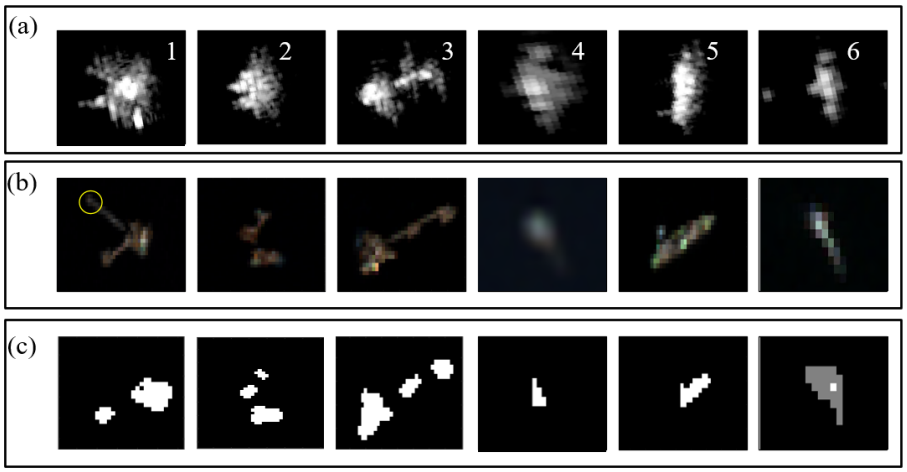

Fig. 9. The different kinds of offshore infrastructure in Sentinel-1 (a), Sentinel-2 (b) and detection results (c).

VI. Conclusion

In this paper, we have proposed an automatic method for the geolocating and measuring of offshore energy infrastructure by leveraging multimodal satellite data, i.e., Sentinel-1 SAR and Sentinel-2 MSI data. First, we demonstrate by using the complementary strengths of SAR and MSI data, our method can produce highly accurate geolocation of the offshore energy infrastructure in Scottish waters, specifically diverse rigs within interconnected oil/gas platforms. With a remarkable detection accuracy of 99.70% achieved for 333 offshore infrastructures, our method has successfully extracted all single oil/gas platforms, wind turbines, and nearly all rigs within linked oil/gas platforms with only a single omission observed. Second, the proposed classification model, which utilizes the minor axis and circularity of the 'guided area', has proven to be very effective in distinguishing the wind turbines from other offshore energy infrastructure. As a result, the model enables automated size measurements, allowing for independent measurement of the topside area size of oil/gas platforms and semi-permanent objects, as well as the diameter length of wind turbines. The size errors for wind turbines, oil/gas platforms and semi-permanent objects are around 1, 1 and 8 pixels, respectively in the Sentinel-2 images, while the size error rate is less than 10% for most of the structures. To sum up, our proposed method has realized automatic geolocation and size measurement of different kinds of offshore energy infrastructure. The experimental results have demonstrated its efficacy in automatic offshore infrastructure detection and evaluation in a vast sea area, which has met the needs for practical applications.

References

[1] P. E. Posen *et al*, "Evaluating differences in marine spatial data resolution and robustness: A North Sea case study," *Ocean Coast. Manage.,* vol. 192, pp. 105206, 2020.

[2] B. J. Williamson *et al*, "A self-contained subsea platform for acoustic monitoring of the environment around Marine Renewable Energy Devices–Field deployments at wave and tidal energy sites in Orkney, Scotland," *IEEE J. Ocean. Eng.,* vol. 41*,* pp. 67-81, 2015.

[3] T. Zhang *et al*, "Global offshore wind turbine dataset," *Sci. Data,* vol. 8, pp. 191, 2021.

[4] V. Parente *et al*, "Offshore decommissioning issues: Deductibility and transferability," *Energ. Policy,* vol. 34, pp. 1992-2001, 2006.

[5] Y. Wang and H. Liu, "A hierarchical ship detection scheme for high-resolution SAR images," *IEEE Trans. Geosci. Remote Sens.,* vol. 50, pp. 4173-4184, 2012.

[6] B. A. Wong, C. Thomas and P. Halpin, "Automating offshore infrastructure extractions using synthetic aperture radar & Google Earth Engine," *Remote Sens. Environ.,* vol. 233, pp. 111412, 2019.

[7] Y. Liu *et al*, "Automatic extraction of offshore platforms using time-series Landsat-8 Operational Land Imager data," *Remote Sens. Environ.,* vol. 175, pp. 73-91, 2016.

[8] J. Li *et al*, "Deep learning in multimodal remote sensing data fusion: A comprehensive review," *Int. J. Appl. Earth Obs. Geoinf.,* vol. 112, pp. 102926, 2022.

[9] G. Benassai *et al*, "Marine spatial planning using high-resolution synthetic aperture radar measurements," *IEEE J. Ocean. Eng.,* vol. 43, pp. 586-594, 2018.

[10] W. Gao *et al*, "Monitoring terrain elevation of intertidal wetlands by utilising the spatial-temporal fusion of multi-source satellite data: A case study in the Yangtze (Changjiang) Estuary," *Geomorph.,* vol. 383, pp. 107683, 2021.

[11] Q. Zhao *et al*, "An overview of the applications of earth observation satellite data: impacts and future trends," *Remote Sens.,* vol. 14*,* pp. 1863, 2022.

[12] S. Zhao *et al*, "Extraction and Monitoring of Offshore Oil and Gas Platforms Based on Landsat Imagery," *Trop. Geogr.*, vol. 37, pp. 112-119, 2017.

[13] Z. Zhu, Y. Tang and T. Han, "Offshore platform detection based on harris detector and intensity-texture image from Sentinel_2A image," in *2018 10th IAPR Workshop on Pattern Recognition in Remote Sensing (PRRS)*, Beijing, China, pp. 1-4, 2018.

[14] W. Xu *et al*, "Proliferation of offshore wind farms in the North Sea and surrounding waters revealed by satellite image time series," *Renew. Sustain. Energy Rev.,* vol. 133, pp. 110167, 2020.

[15] H. Zhu *et al*, "Detecting Offshore Drilling Rigs with Multitemporal NDWI: A Case Study in the Caspian Sea," *Remote Sens.,* vol. 13, pp. 1576, 2021.

[16] T. A. Croft, "Nighttime images of the earth from space," *Sci. Am.,* vol. 239, pp. 86-101, 1978.

[17] S. Casadio, O. Arino and A. Minchella, "Use of ATSR and SAR measurements for the monitoring and characterisation of night-time gas flaring from off-shore platforms: The North Sea test case," *Remote Sens. Environ.,* vol. 123, pp. 175-186, 2012.

[18] O. C. Anejionu, G. A. Blackburn and J. D. Whyatt, "Detecting gas flares and estimating flaring volumes at individual flow stations using MODIS data," *Remote Sens. Environ.,* vol. 158, pp. 81-94, 2015.

[19] C. D. Elvidge *et al*, "Methods for global survey of natural gas flaring from visible infrared imaging radiometer suite data," *Energies,* vol. 9, pp. 14, 2015.

[20] C. D. Elvidge *et al*, "VIIRS nightfire: Satellite pyrometry at night," *Remote Sens.,* vol. 5, pp. 4423-4449, 2013.

[21] L. Cheng *et al*, "Invariant triangle-based stationary oil platform detection from multitemporal synthetic aperture radar data," *J. Appl. Remote Sens.,* vol. 7, pp. 073537, 2013.

[22] W. An, M. Lin and H. Yang, "Stationary Marine Target Detection with Time-Series SAR Imagery," *IEEE J. Sel. Top. Appl. Earth Obs. Remote Sens.,* vol. 14, pp. 6406-6413, 2021.

[23] F. Nunziata and M. Migliaccio, "On the COSMO-SkyMed PingPong Mode to Observe Metallic Targets at Sea," *IEEE J. Ocean. Eng.,* vol. 38, pp. 71-79, 2013.

[24] Z. Xu *et al*, "Dynamic detection of offshore wind turbines by spatial machine learning from spaceborne synthetic aperture radar imagery," *J. King Saud Univ. - Comput. Inf. Sci.,* vol. 34, pp. 1674-1686, 2022.

[25] Y. Liu *et al*, "Assessment of offshore oil/gas platform status in the northern Gulf of Mexico using multi-source satellite time-series images," *Remote Sens. Environ.,* vol. 208, pp. 63-81, 2018.

[26] A. Marino, D. Velotto and F. Nunziata, "Offshore Metallic Platforms Observation Using Dual-Polarimetric TS-X/TD-X Satellite Imagery: A Case Study in the Gulf of Mexico," *IEEE J. Sel. Top. Appl. Earth Obs. Remote Sens.,* vol. 10, pp. 4376-4386, 2017.

[27] Y. Liu *et al*, "Geometric accuracy of remote sensing images over oceans: The use of global offshore platforms," *Remote Sens. Environ.,* vol. 222, pp. 244-266, 2019.

[28] T. Hoeser, S. Feuerstein and C. Kuenzer, "DeepOWT: A global offshore wind turbine data set derived with deep learning from Sentinel-1 data," *Earth Syst. Sci. Data,* vol. 14, pp. 4251-4270, 2022.

[29] United Kingdom Hydrographic Office (UKHO), 2013, "Scottish Zone (200M Limit) - Exclusive Economic Zone (EEZ) adjacent to Scotland - Exclusive Economic Zone (EEZ) Order 2013," accessed 31st, December, 2021; https://marine.gov.scot/maps/416.

[30] European Marine Observation and Data Network (EMODnet), 2020, "The Scotland coastline," accessed 15th, January, 2022; https://www.emodnet-bathymetry.eu/media/emodnet_bathymetry/org/documents/emodnet_coastline_and_baseline_collection_2020-18dec2020.pdf.

[31] OSPAR Commission, 2019, "OSPAR Inventory of Offshore Installations - 2019," accessed 31st, December, 2021; https://odims.ospar.org/en/submissions/ospar_offshore_installations_2019_01/.

[32] Oil and Gas Authority, 2021, "Offshore Oil and Gas Activity," accessed 4th, January, 2022; https://ogauthority.maps.arcgis.com/apps/webappviewer/index.html?id=adbe5a796f5c41c68fc762ea137a682e.

[33] European Space Agency, 2017, "EO Browser," accessed 4th, January, 2022; https://www.sentinel-hub.com/explore/eobrowser/.

[34] Marine Scotland, 2015, "Beatrice Offshore Wind Farm Consent Plan," accessed 2nd, January, 2022; https://marine.gov.scot/sites/default/files/00510248.pdf.

[35] Marine Scotland, 2018, "Development Layout and Specification Plan — Moray East Offshore Wind Farm and Associated Offshore Transmission Infrastructure.," accessed 15th January 2022; https://marine.gov.scot/sites/default/files/moray_east_dslp_version_2_final_aug_2018.pdf.

[36] Marine Scotland, 2017, "The Design Statement for Aberdeen Offshore Wind Farm," accessed 15th January 2022; https://marine.gov.scot/sites/default/files/00518408.pdf

[37] Marine Scotland, 2017, "Hywind Scotland Pilot Park Project Plan for Construction Activities," accessed 7th February 2022; https://marine.gov.scot/sites/default/files /00516548_0.pdf.

[38] Marine Scotland, 2023, " Kincardine Offshore Windfarm - Development Specification and Layout Plan," accessed 10th July 2023; https://marine.gov.scot/data/kincardine-offshore-windfarm-development-specification-and-layout-plan-dslp

[39] A. Shelestov *et al*, "Cloud Approach to Automated Crop Classification Using Sentinel-1 Imagery," *IEEE Trans. Big Data,* vol. 6*,* pp. 572-582, 2020.

[40] European Space Agency, 2021, " Revisit and Coverage," accessed 10th September 2023; https://sentinels.copernicus.eu/web/sentinel/user-guides/sentinel-1-sar/revisit-and-coverage

[41] European Space Agency, 2022, "Mission ends for Copernicus Sentinel-1B satellite," accessed 10th September 2023; https://www.esa.int/Applications/Observing_the_Earth/Copernicus/Sentinel-1/Mission_ends_for_Copernicus_Sentinel-1B_satellite

[42] J. Zabalza *et al*, "Novel Two-Dimensional Singular Spectrum Analysis for Effective Feature Extraction and Data Classification in Hyperspectral Imaging," *IEEE Trans. Geosci. Remote Sens.,* vol. 53, pp. 4418-4433, 2015.

[43] N. Otsu, "A thresholding selection method from gray-level histogram," *IEEE SMC-8*, pp. 62-66, 1978.

[44] E. Grosso and R. Guida, "A New Automated Ship Wake Detector for Small and Go-Fast Ships in Sentinel-1 Imagery," *Remote Sens.,* vol. 14, pp. 6223, 2022.

[45] X. Luo, X. Tong and H. Pan, "Integrating multiresolution and multitemporal Sentinel-2 imagery for land-cover mapping in the Xiongan New Area, China," *IEEE Trans. Geosci. Remote Sens.,* vol. 59, pp. 1029-1040, 2020.

[46] B. Han, "Watershed segmentation algorithm based on morphological gradient reconstruction," in *2015 2nd International Conference on Information Science and Control Engineering*, Shanghai, China, pp. 533-536, 2015.

[47] J. Serra, "Mathematical morphology," in *Encyclopedia of Mathematical Geosciences*, Cham: Springer International Publishing, pp. 1-16. 2022.

Supplementary Materials

Automatic Geolocation and Measuring of Offshore Energy Infrastructure with Multimodal Satellite Data

Ping Ma, Malcolm Macdonald, Sally Rouse, Jinchang Ren

Tables

Table S1. The constructed ground truth dataset of oil/gas platforms and semi-permanent objects.

ID	Name	Latitude (°)	Longitude (°)	Topside area (Square meters)
1	Dunbar	60.6286	1.6510	4428
2	Magnus	61.6198	1.3050	8532
3	Western Isles FPSO	61.2140	0.7540	6460
4	Tern	61.2751	0.9180	4950
5	Heather Alpha	60.9530	0.9380	4290
6	Cormorant Alpha	61.1020	1.0710	6984
7	North Cormorant	61.2400	1.1480	4600
8	Eider	61.3565	1.1600	3818
9	Ninian north *	60.9054	1.4195	—
10	Ninian South	60.8050	1.4490	7199
11	Northern Producer *	61.4870	1.4630	—
12	Ninian Central	60.8560	1.4680	8840
13	Thistle Alpha	61.3620	1.5780	6460
14	Dunlin Alpha	61.2742	1.5958	6840
15	Brent Bravo *	61.0550	1.7110	—
16	Brent Charlie	61.0959	1.7200	7878

17	Alwyn North Bravo	60.8096	1.7340	3551
18	Alwyn North Alpha	60.8086	1.7360	3927
19	Brent Delta *	61.1320	1.7341	—
20	Noble Lloyd Noble	59.5891	1.0550	4728
21	Mariner production, drilling and living quarters (PDQ)	59.5880	1.0550	10295
22	Mariner floating storage unit (FSU)	59.6085	1.0760	10130
23	Kraken FPSO	59.9258	1.2930	12502
24	Beryl Bravo	59.6099	1.5110	4689
25	Harding	59.2790	1.5140	5304
26	Beryl Alpha	59.5446	1.5340	1406
27	Beryl Flare	59.5460	1.5330	378
28	Beryl Alpha Riser	59.5450	1.5360	6935
29	Beryl Single Point Mooring (SPM)-3	59.5338	1.5575	1364
30	Beryl Single Point Mooring (SPM)-2	59.5535	1.5610	2179
31	Gryphon Alpha FPSO	59.3600	1.5690	10500
32	Bruce Process, Utilities and Quarters (PUQ)	59.7421	1.6710	4698
33	Bruce Compression Reception (CR)	59.7438	1.6710	706
34	Bruce Drilling	59.7430	1.6700	1890
35	Tartan Alpha	58.3692	0.0720	4042
36	Scott Drilling and Process (DP)	58.2887	0.2006	3080
37	Scott Utilities and Quarters (UQ).	58.2883	0.1990	3968
38	Piper Bravo	58.4607	0.2494	6090
39	Saltire	58.4163	0.3331	3726
40	Global Producer III FPSO	58.3529	0.8630	8660
41	Alba FPSO	58.0478	1.0329	9089
42	Alba North	58.0580	1.0800	4080
43	Balmoral FPSO	58.2287	1.1071	5010
44	Britannia	58.0480	1.1372	6032
45	Britannia Bridge-Linked Platform (BLP)	58.0481	1.1400	2279
46	Hummingbird FPSO	57.9760	1.2380	4154
47	Tiffany	58.4777	1.2649	4988

48	Brae Alpha	58.6920	1.2803	5427
49	Brae Bravo	58.7916	1.3458	4140
50	Andrew	58.0469	1.4027	4264
51	Brae East	58.8755	1.5254	4088
52	Glen Lyon FPSO	60.3560	-4.0680	13993
53	Solan	60.0618	-3.9710	1856
54	Aoka Mizu FPSO	60.1800	-3.8700	9945
55	Clair	60.6920	-2.5440	6627
56	Clair Ridge DP	60.7361	-2.4940	5972
57	Clair Ridge quarters and utilities (QU)	60.7360	-2.4970	5151
58	Foinaven FPSO	60.3150	-4.2760	8800
59	Claymore Production	58.4490	-0.2565	3127
60	Claymore Accommodation	58.4489	-0.2556	2546
61	Captain BLP	58.3060	-1.7714	2236
62	Captain wellhead protection platform (WPP)	58.3070	-1.7700	3927
63	Captain FPSO	58.3052	-1.7436	7562
64	Ross FPSO	58.1015	-1.4400	9009
65	Well Head	57.8140	-0.9740	2583
66	Production Jacket	57.8138	-0.9760	3440
67	Quarters Utilities (QU) Jacket	57.8130	-0.9780	3502
68	Oil Stripper platform (PS)	57.8144	-0.9762	2107
69	Golden Eagle Wellhead	57.9610	-0.9180	2695
70	Golden Eagle PUQ	57.9600	-0.9180	4059
71	Kittiwake	57.4678	0.5102	3832
72	Catcher FPSO	56.7700	0.7130	11050
73	Forties Unity	57.7210	0.7548	1815
74	Anasuria FPSO	57.2565	0.8081	9072
75	Forties Charlie	57.7260	0.8460	5760
76	Triton FPSO	57.0831	0.8910	9460
77	Forties Delta	57.7219	0.9010	6083
78	Forties Bravo	57.7485	0.9134	4180

79	Forties Alpha	57.7310	0.9710	5616
80	Fasp	57.7310	0.9689	3036
81	Gannet Alpha	57.1843	0.9984	4158
82	Forties Echo	57.7157	1.0310	2132
83	Nelson	57.6627	1.1446	5346
84	Arbroath	57.3743	1.3816	2304
85	Montrose BLP	57.4510	1.3870	2916
86	Montrose Alpha	57.4501	1.3870	4104
87	Etap processing, drilling and riser (PDR)	57.2941	1.6620	2666
88	Etap QU	57.2937	1.6610	3256
89	North Everest	57.7580	1.8000	3440
90	Cats Riser	57.7575	1.8020	1122
91	West Franklin wellhead platform (WHP)	56.9592	1.8060	2352
92	Elgin A WHP	57.0116	1.8383	1890
93	Elgin B WHP	57.0112	1.8402	6561
94	Elgin PUQ	57.0110	1.8362	3129
95	Franklin WHP	56.9660	1.8680	6520
96	Culzean Utilities and Living Quarters (ULQ)	57.1902	1.9079	2960
97	Culzean Central Processing Facility (CPF)	57.1910	1.9100	3042
98	Culzean WHP	57.1921	1.9110	5920
99	Shearwater A	57.0315	1.9538	4860
100	Shearwater C	57.0303	1.9534	3564
101	Erskine	57.0390	2.0700	2028
102	FPF1 FPSO	56.7810	2.1090	6525
103	Mungo	57.3747	1.9965	2090
104	Lomond	57.2869	2.1767	3276
105	Jasmine Wellhead	56.7242	2.2060	7112
106	Jasmine Living Quarters (JLQ)	56.7235	2.2040	2180
107	Jade	56.8490	2.2540	2108
108	Haewene Brim FPSO	57.1609	2.2930	6534
109	Judy Riser and Separation Platform (JRP)	56.6980	2.3350	4176

110	Judy	56.6968	2.3369	5775
111	Culzean FSO - Ailsa	57.1955	1.9610	8697
112	Armada	57.9567	1.8444	4699
113	Jacky platform	58.1838	-2.9801	5102
114	Beatrice Charlie *	58.0940	-3.1532	—
115	Betrice Alpha Drilling *	58.1148	-3.0880	—
116	Beatrice Alpha Production *	58.1140	-3.0890	—
117	Beatrice Bravo *	58.1473	-3.0216	—
118	Manifold and Compression Platform 01 (MCP01) *	58.8265	-0.2880	—
119	Frigg Treatment platform 1 (TP1) *	59.8790	2.0630	—
120	Frigg Concrete drilling platform 1 (CDP1) *	59.8748	2.0607	—
121	Frigg Treatment Compression Platform 2 (TCP 2) *	59.8791	2.0650	—

* The infrastructure has undergone decommissioning.

Table S2. The constructed ground truth dataset of wind turbines in Beatrice Wind Farm.

ID	Name	Latitude (˚)	Longitude (˚)	Diameter Length (Meters)
1	BE-A5	58.2079	-2.9999	154
2	BE-B5	58.2115	-2.9812	154
3	BE-B6	58.2218	-2.9777	154
4	BE-B7	58.2322	-2.9743	154
5	BE-C4	58.2051	-2.9656	154
6	BE-C5	58.2150	-2.9625	154
7	BE-C6	58.2254	-2.9590	154
8	BE-C7	58.2357	-2.9555	154
9	BE-C8	58.2461	-2.9521	154
10	BE-C9	58.2564	-2.9486	154
11	BE-D3	58.1999	-2.9500	154
12	BE-D4	58.2083	-2.9472	154
13	BE-D5	58.2186	-2.9438	154

14	BE-D6	58.2289	-2.9403	154
15	BE-D7	58.2393	-2.9368	154
16	BE-D8	58.2497	-2.9333	154
17	BE-D9	58.2600	-2.9298	154
18	BE-D10	58.2704	-2.9264	154
19	BE-D11	58.2807	-2.9229	154
20	BE-E1	58.1817	-2.9375	154
21	BE-E2	58.1912	-2.9355	154
22	BE-E3	58.2015	-2.9320	154
23	BE-E4	58.2119	-2.9285	154
24	BE-E5	58.2222	-2.9250	154
25	BE-E6	58.2326	-2.9216	154
26	BE-E7	58.2429	-2.9181	154
27	BE-E8	58.2533	-2.9146	154
28	BE-E9	58.2636	-2.9111	154
29	BE-E10	58.2739	-2.9076	154
30	BE-E11	58.2843	-2.9041	154
31	BE-E12	58.2947	-2.9006	154
32	BE-F2	58.1948	-2.9168	154
33	BE-F3	58.2051	-2.9133	154
34	BE-F4	58.2155	-2.9098	154
35	BE-F5	58.2258	-2.9063	154
36	BE-F6	58.2361	-2.9028	154
37	BE-F9	58.2672	-2.8923	154
38	BE-F10	58.2776	-2.8888	154
39	BE-F11	58.2879	-2.8853	154
40	BE-F12	58.2982	-2.8819	154
41	BE-F13	58.3086	-2.8784	154
42	BE-G3	58.2091	-2.8954	154
43	BE-G4	58.2190	-2.8911	154
44	BE-G5	58.2293	-2.8876	154

45	BE-G6	58.2397	-2.8841	154
46	BE-G8	58.2604	-2.8771	154
47	BE-G9	58.2708	-2.8736	154
48	BE-G10	58.2811	-2.8701	154
49	BE-G11	58.2915	-2.8666	154
50	BE-G12	58.3018	-2.8631	154
51	BE-G13	58.3122	-2.8596	154
52	BE-G14	58.3225	-2.8560	154
53	BE-H4	58.2226	-2.8723	154
54	BE-H5	58.2329	-2.8688	154
55	BE-H6	58.2433	-2.8653	154
56	BE-H7	58.2537	-2.8618	154
57	BE-H8	58.2640	-2.8583	154
58	BE-H9	58.2744	-2.8548	154
59	BE-H10	58.2847	-2.8513	154
60	BE-H11	58.2951	-2.8478	154
61	BE-H12	58.3054	-2.8443	154
62	BE-H13	58.3157	-2.8408	154
63	BE-J5	58.2365	-2.8501	154
64	BE-J6	58.2469	-2.8466	154
65	BE-J7	58.2572	-2.8431	154
66	BE-J8	58.2676	-2.8396	154
67	BE-J9	58.2779	-2.8361	154
68	BE-J10	58.2883	-2.8325	154
69	BE-J11	58.2986	-2.8290	154
70	BE-J12	58.3089	-2.8255	154
71	BE-J13	58.3193	-2.8219	154
72	BE-K6	58.2505	-2.8278	154
73	BE-K7	58.2608	-2.8243	154
74	BE-K8	58.2712	-2.8208	154
75	BE-K9	58.2815	-2.8173	154

76	BE-K10	58.2918	-2.8138	154
77	BE-K11	58.3022	-2.8102	154
78	BE-K12	58.3125	-2.8067	154
79	BE-L7	58.2644	-2.8056	154
80	BE-L8	58.2747	-2.8020	154
81	BE-L9	58.2851	-2.7985	154
82	BE-L10	58.2954	-2.7949	154
83	BE-M9	58.2886	-2.7797	154
84	BE-M10	58.2989	-2.7762	154
85	Wind turbine A	58.0999	-3.0827	154
86	Wind turbine B	58.0955	-3.0739	154
87	BE-F8*	58.2567	-2.8956	—
88	BE-G7*	58.2497	-2.8803	—

* Offshore transformer modules (OTMs)

Table S3. The constructed ground truth dataset of wind turbines in Moray East Wind Farm.

ID	Name	Latitude (°)	Longitude (°)	Diameter Length (Meters)
1	ME-A01	58.0758	-2.8691	164
2	ME-A02	58.0859	-2.8691	164
3	ME-B02	58.0858	-2.8428	164
4	ME-B03	58.0959	-2.8428	164
5	ME-B04	58.1061	-2.8427	164
6	ME-B05	58.1161	-2.8424	164
7	ME-B13	58.1973	-2.8423	164
8	ME-B14	58.2074	-2.8423	164
9	ME-C02	58.0855	-2.8166	164
10	ME-C04	58.1059	-2.8165	164
11	ME-C05	58.1160	-2.8164	164
12	ME-C07	58.1363	-2.8163	164
13	ME-C08	58.1464	-2.8163	164

14	ME-C09	58.1566	-2.8162	164
15	ME-C10	58.1667	-2.8162	164
16	ME-C11	58.1768	-2.8162	164
17	ME-C12	58.1869	-2.8161	164
18	ME-C13	58.1971	-2.8161	164
19	ME-C14	58.2073	-2.8159	164
20	ME-C15	58.2174	-2.8159	164
21	ME-C16	58.2275	-2.8159	164
22	ME-D04	58.1057	-2.7902	164
23	ME-D05	58.1158	-2.7902	164
24	ME-D06	58.1258	-2.7901	164
25	ME-D07	58.1361	-2.7901	164
26	ME-D08	58.1462	-2.7899	164
27	ME-D09	58.1564	-2.7899	164
28	ME-D10	58.1665	-2.7899	164
29	ME-D11	58.1766	-2.7898	164
30	ME-D12	58.1868	-2.7897	164
31	ME-D13	58.1969	-2.7898	164
32	ME-D14	58.2071	-2.7896	164
33	ME-D15	58.2171	-2.7896	164
34	ME-D16	58.2273	-2.7895	164
35	ME-D17	58.2375	-2.7895	164
36	ME-E04	58.1055	-2.7639	164
37	ME-E05	58.1156	-2.7639	164
38	ME-E14	58.2069	-2.7633	164
39	ME-E18	58.2474	-2.7630	164
40	ME-E19	58.2575	-2.7629	164
41	ME-F04	58.1053	-2.7377	164
42	ME-F08	58.1458	-2.7374	164
43	ME-F21	58.2776	-2.7365	164
44	ME-G05	58.1152	-2.7114	164

45	ME-G06	58.1254	-2.7113	164
46	ME-G07	58.1355	-2.7112	164
47	ME-G08	58.1456	-2.7111	164
48	ME-G09	58.1558	-2.7111	164
49	ME-G10	58.1659	-2.7109	164
50	ME-G11	58.1760	-2.7109	164
51	ME-G13	58.1963	-2.7107	164
52	ME-G15	58.2166	-2.7106	164
53	ME-G16	58.2267	-2.7105	164
54	ME-G17	58.2369	-2.7104	164
55	ME-G18	58.2469	-2.7103	164
56	ME-G19	58.2571	-2.7102	164
57	ME-G20	58.2673	-2.7102	164
58	ME-G21	58.2774	-2.7101	164
59	ME-G22	58.2875	-2.7099	164
60	ME-H05	58.1150	-2.6851	164
61	ME-H06	58.1251	-2.6850	164
62	ME-H07	58.1352	-2.6849	164
63	ME-H08	58.1454	-2.6849	164
64	ME-H09	58.1556	-2.6848	164
65	ME-H10	58.1657	-2.6847	164
66	ME-H11	58.1758	-2.6846	164
67	ME-H13	58.1961	-2.6844	164
68	ME-H14	58.2062	-2.6843	164
69	ME-H16	58.2265	-2.6841	164
70	ME-H17	58.2366	-2.6840	164
71	ME-H18	58.2468	-2.6839	164
72	ME-H19	58.2569	-2.6839	164
73	ME-H20	58.2671	-2.6838	164
74	ME-H21	58.2772	-2.6837	164
75	ME-H22	58.2873	-2.6836	164

76	ME-I06	58.1249	-2.6588	164
77	ME-I07	58.1351	-2.6587	164
78	ME-I18	58.2466	-2.6576	164
79	ME-I19	58.2567	-2.6575	164
80	ME-I20	58.2668	-2.6574	164
81	ME-J07	58.1348	-2.6324	164
82	ME-J08	58.1449	-2.6323	164
83	ME-J09	58.1551	-2.6322	164
84	ME-J10	58.1652	-2.6321	164
85	ME-J12	58.1855	-2.6319	164
86	ME-J13	58.1957	-2.6318	164
87	ME-J14	58.20583	-2.6317	164
88	ME-J16	58.2261	-2.6314	164
89	ME-J17	58.2362	-2.6313	164
90	ME-J18	58.2463	-2.6312	164
91	ME-J19	58.2564	-2.6315	164
92	ME-K09	58.1549	-2.6059	164
93	ME-K10	58.1650	-2.6058	164
94	ME-K11	58.1752	-2.6057	164
95	ME-K16	58.2258	-2.6051	164
96	ME-K17	58.2365	-2.6022	164
97	ME-L09	58.1546	-2.5796	164
98	ME-L11	58.1749	-2.5794	164
99	ME-L12	58.1851	-2.5792	164
100	ME-L13	58.1952	-2.5791	164
101	OSP1*	58.1257	-2.7641	—
102	OSP2*	58.2167	-2.7371	—
103	OSP3*	58.1654	-2.6585	—

* Offshore Substation Platform (OSP)

Table S4. The constructed ground truth dataset of wind turbines in HyWind Wind Farm (Aberdeenshire).

ID	Name	Latitude (˚)	Longitude (˚)	Diameter Length (Meters)
1	HS1	57.4843	-1.3323	154
2	HS2	57.4908	-1.3520	154
3	HS3	57.4972	-1.3718	154
4	HS4	57.4783	-1.3526	154
5	HS5	57.4848	-1.3723	154

Table S5. The constructed ground truth dataset of wind turbines in Kincardine Wind Farm (Aberdeenshire).

ID	Name	Latitude (˚)	Longitude (˚)	Diameter Length (Meters)
1	KIN-01	57.0053	-1.8812	164
2	KIN-02	56.9973	-1.8738	164
3	KIN-03	56.9892	-1.8665	164
4	KIN-04	57.0186	-1.8550	164
5	KIN-05	57.0105	-1.8477	164

Table S6. The constructed ground truth dataset of wind turbines in Aberdeen Offshore Wind Farm.

ID	Name	Latitude (˚)	Longitude (˚)	Diameter Length (Meters)
1	AWF01	57.2237	-2.0126	150
2	AWF02	57.2284	-2.0022	150
3	AWF03	57.2335	-1.9895	150
4	AWF04	57.2401	-1.9758	150
5	AWF05	57.2158	-2.0112	150
6	AWF06	57.2201	-2.0002	150
7	AWF07	57.2244	-1.9879	150
8	AWF08	57.2301	-1.9742	150
9	AWF09	57.2079	-2.0104	150

10	AWF10	57.2117	-1.9987	150
11	AWF11	57.2160	-1.9858	150

Table S7. The detected contour range results of oil/gas platforms and semi-permanent objects in Scottish waters.

ID	Name	Contour range	
		Latitude (°)	Longitude (°)
1	Dunbar	60.628517 ~ 60.629055	1.649901 ~ 1.651715
2	Magnus	61.619080 ~ 61.619962	1.304405 ~ 1.306393
3	Western Isles FPSO	61.213852 ~ 61.214820	0.753038 ~ 0.754490
4	Tern	61.274986 ~ 61.275689	0.917036 ~ 0.918669
5	Heather Alpha	60.952831 ~ 60.953364	0.937178 ~ 0.938630
6	Cormorant Alpha	61.101560 ~ 61.102532	1.070591 ~ 1.072043
7	North Cormorant	61.239452 ~ 61.240244	1.147276 ~ 1.148546
8	Eider	61.356320 ~ 61.356846	1.159268 ~ 1.160539
9	Ninian north	60.905220 ~ 60.905576	1.419303 ~ 1.419848
10	Ninian South	60.804512 ~ 60.805404	1.447774 ~ 1.449770
11	Northern Producer	61.486624 ~ 61.487322	1.461770 ~ 1.463403
12	Ninian Central	60.855808 ~ 60.856432	1.466477 ~ 1.468473
13	Thistle Alpha	61.361894 ~ 61.362771	1.577503 ~ 1.578954
14	Dunlin Alpha	61.273705 ~ 61.274584	1.595310 ~ 1.596762
15	Brent Bravo	61.054543 ~ 61.056136	1.710742 ~ 1.712193
16	Brent Charlie	61.095037 ~ 61.095921	1.719479 ~ 1.721112
17	Alwyn North Bravo	60.809090 ~ 60.809723	1.733229 ~ 1.734314
18	Alwyn North Alpha	60.808365 ~ 60.808818	1.735217 ~ 1.736482
19	Brent Delta	61.131771 ~ 61.132125	1.734055 ~ 1.734418
20	Noble Lloyd Noble	59.589025 ~ 59.589847	1.053823 ~ 1.055274
21	Mariner production, drilling and living quarters (PDQ)	59.587837 ~ 59.588751	1.053097 ~ 1.056000
22	Mariner floating storage unit (FSU)	59.607397 ~ 59.608524	1.073946 ~ 1.077199
23	Kraken FPSO	59.924172 ~ 59.925939	1.291559 ~ 1.293367

24	Beryl Bravo	59.609422 ~ 59.609977	1.510435 ~ 1.511705
25	Harding	59.278428 ~ 59.279268	1.513581 ~ 1.515214
26	Beryl Alpha	59.544489 ~ 59.544677	1.533876 ~ 1.534418
27	Beryl Flare*	—	—
28	Beryl Alpha Riser	59.544677 ~ 59.545336	1.535502 ~ 1.536948
29	Beryl Single Point Mooring (SPM)-3	59.533681 ~ 59.533867	1.557417 ~ 1.557780
30	Beryl Single Point Mooring (SPM)-2	59.553452 ~ 59.553822	1.560377 ~ 1.561465
31	Gryphon Alpha FPSO	59.359063 ~ 59.361206	1.568349 ~ 1.570707
32	Bruce Process, Utilities and Quarters (PUQ)	59.742005 ~ 59.742557	1.670322 ~ 1.671955
33	Bruce Compression Reception (CR) *	—	—
34	Bruce Drilling	59.742834 ~ 59.743202	1.669960 ~ 1.670686
35	Tartan Alpha	58.368864 ~ 58.369439	0.071343 ~ 0.072976
36	Scott Drilling and Process (DP)	58.288221 ~ 58.288904	0.199949 ~ 0.200853
37	Scott Utilities and Quarters (UQ).	58.287928 ~ 58.288513	0.198323 ~ 0.199408
38	Piper Bravo	58.460123 ~ 58.461079	0.248381 ~ 0.250377
39	Saltire	58.415647 ~ 58.416509	0.331739 ~ 0.333191
40	Global Producer III FPSO	58.352599 ~ 58.352989	0.860096 ~ 0.863891
41	Alba FPSO	58.047390 ~ 58.047874	1.031359 ~ 1.032992
42	Alba North	58.057568 ~ 58.058342	1.078810 ~ 1.080625
43	Balmoral FPSO	58.228229 ~ 58.228893	1.106116 ~ 1.107925
44	Britannia	58.047547 ~ 58.048235	1.135946 ~ 1.138115
45	Britannia Bridge-Linked Platform (BLP)	58.047842 ~ 58.048235	1.139018 ~ 1.140103
46	Hummingbird FPSO	57.975876 ~ 57.976555	1.237036 ~ 1.238125
47	Tiffany	58.477197 ~ 58.478057	1.263989 ~ 1.265804
48	Brae Alpha	58.691522 ~ 58.692282	1.279512 ~ 1.281145
49	Brae Bravo	58.791158 ~ 58.791916	1.345040 ~ 1.346492
50	Andrew	58.046424 ~ 58.047198	1.401684 ~ 1.403498
51	Brae East	58.874968 ~ 58.875724	1.524741 ~ 1.526011
52	Glen Lyon FPSO	60.354990 ~ 60.356618	-4.068720 ~ -4.064214
53	Solan	60.061161 ~ 60.061891	-3.971589 ~ -3.970327
54	Aoka Mizu FPSO	60.179083 ~ 60.180174	-3.870801 ~ -3.866655

55	Clair	60.691568 ~ 60.692121	-2.545760 ~ -2.543563
56	Clair Ridge DP	60.736072 ~ 60.736809	-2.495225 ~ -2.493211
57	Clair Ridge quarters and utilities (QU)	60.735611 ~ 60.736072	-2.498155 ~ -2.496141
58	Foinaven FPSO	60.314613 ~ 60.316062	-4.276289 ~ -4.272143
59	Claymore Production	58.448721 ~ 58.449486	-0.258089 ~ -0.256457
60	Claymore Accommodation	58.448147 ~ 58.448912	-0.255731 ~ -0.254099
61	Captain BLP	58.305752 ~ 58.306226	-1.771938 ~ -1.771031
62	Captain wellhead protection platform (WPP)	58.306416 ~ 58.307175	-1.770669 ~ -1.769580
63	Captain FPSO	58.304506 ~ 58.305299	-1.747163 ~ -1.743501
64	Ross FPSO	58.100758 ~ 58.102698	-1.441461 ~ -1.439834
65	Well Head	57.813932 ~ 57.814427	-0.975030 ~ -0.973946
66	Production Jacket	57.813141 ~ 57.813834	-0.976657 ~ -0.975030
67	Quarters Utilities (QU) Jacket	57.812350 ~ 57.813043	-0.978644 ~ -0.976837
68	Oil Stripper platform (PS)	57.814229 ~ 57.814723	-0.976657 ~ -0.975753
69	Golden Eagle Wellhead	57.960820 ~ 57.961411	-0.918163 ~ -0.916899
70	Golden Eagle PUQ	57.959540 ~ 57.960328	-0.918705 ~ -0.917260
71	Kittiwake	57.467124 ~ 57.467834	0.510031 ~ 0.511130
72	Catcher FPSO	56.769782 ~ 56.770384	0.709836 ~ 0.713645
73	Forties Unity	57.720689 ~ 57.721177	0.754255 ~ 0.754981
74	Anasuria FPSO	57.256170 ~ 57.256665	0.804706 ~ 0.808153
75	Forties Charlie	57.725894 ~ 57.726577	0.845140 ~ 0.846591
76	Triton FPSO	57.082713 ~ 57.083310	0.887659 ~ 0.891287
77	Forties Delta	57.721330 ~ 57.722014	0.900881 ~ 0.902152
78	Forties Bravo	57.748255 ~ 57.748938	0.912827 ~ 0.914097
79	Forties Alpha	57.730904 ~ 57.731608	0.970453 ~ 0.971918
80	Fasp	57.730803 ~ 57.731407	0.968622 ~ 0.969538
81	Gannet Alpha	57.183816 ~ 57.185005	0.996785 ~ 0.999325
82	Forties Echo	57.715369 ~ 57.715759	1.030276 ~ 1.031002
83	Nelson	57.661688 ~ 57.662861	1.143109 ~ 1.145468
84	Arbroath	57.373967 ~ 57.374558	1.380932 ~ 1.382021
85	Montrose BLP	57.450681 ~ 57.451480	1.386506 ~ 1.387049

86	Montrose Alpha	57.449583 ~ 57.450381	1.386145 ~ 1.387410
87	Etap processing, drilling and riser (PDR)	57.294031 ~ 57.294525	1.660861 ~ 1.662312
88	Etap QU	57.293142 ~ 57.293834	1.660135 ~ 1.661587
89	North Everest	57.757697 ~ 57.758184	1.799136 ~ 1.800951
90	Cats Riser	57.757209 ~ 57.757599	1.801132 ~ 1.802402
91	West Franklin wellhead platform (WHP)	56.959151 ~ 56.959563	1.805378 ~ 1.806296
92	Elgin A WHP*	—	—
93	Elgin B WHP*	—	—
94	Elgin PUQ	57.010471 ~ 57.011367	1.835573 ~ 1.837387
95	Franklin WHP	56.965817 ~ 56.966537	1.866625 ~ 1.869189
96	Culzean Utilities and Living Quarters (ULQ)	57.189832 ~ 57.190525	1.907131 ~ 1.908583
97	Culzean Central Processing Facility (CPF)	57.190723 ~ 57.191516	1.908764 ~ 1.910215
98	Culzean WHP	57.192011 ~ 57.193200	1.909852 ~ 1.911848
99	Shearwater A	57.031179 ~ 57.032362	1.952427 ~ 1.954420
100	Shearwater C	57.029799 ~ 57.030785	1.952608 ~ 1.954057
101	Erskine	57.038847 ~ 57.039344	2.069724 ~ 2.070450
102	FPF1 FPSO	56.780219 ~ 56.781021	2.108290 ~ 2.109741
103	Mungo	57.374524 ~ 57.374931	1.996159 ~ 1.996892
104	Lomond	57.286520 ~ 57.287112	2.175829 ~ 2.177462
105	Jasmine Wellhead	56.724125 ~ 56.725228	2.204670 ~ 2.206666
106	Jasmine Living Quarters (JLQ)	56.723322 ~ 56.723723	2.203944 ~ 2.204852
107	Jade	56.848831 ~ 56.849330	2.253838 ~ 2.254746
108	Haewene Brim FPSO	57.160319 ~ 57.160914	2.292038 ~ 2.293671
109	Judy Riser and Separation Platform (JRP)	56.697618 ~ 56.698120	2.334940 ~ 2.336210
110	Judy	56.696112 ~ 56.697116	2.336391 ~ 2.337843
111	Culzean FSO - Ailsa	57.195223 ~ 57.195619	1.959675 ~ 1.961490
112	Armada	57.956237 ~ 57.957207	1.843930 ~ 1.844837
113	Jacky platform	58.182816 ~ 58.183866	-2.980600 ~ -2.979338
114	Beatrice Charlie	58.093794 ~ 58.094180	-3.153639 ~ -3.152913
115	Betrice Alpha Drilling	58.114305 ~ 58.114884	-3.088377 ~ -3.086926
116	Beatrice Alpha Production	58.113725 ~ 58.114305	-3.089647 ~ -3.088559

117	Beatrice Bravo	58.147027 ~ 58.147419	-3.022115 ~ -3.021211
118	Manifold and Compression Platform 01 (MCP01)	58.826305 ~ 58.827157	-0.288824 ~ -0.287554
119	Frigg Treatment platform 1 (TP1)	59.878877 ~ 59.879333	2.062646 ~ 2.063191
120	Frigg Concrete drilling platform 1 (CDP1)	59.874407 ~ 59.874863	2.060096 ~ 2.060823
121	Frigg Treatment Compression Platform 2 (TCP 2)	59.879060 ~ 59.879607	2.064642 ~ 2.065550

* The infrastructure is omitted in Sentinel-2 data.

Table S8. The detected contour range results in Beatrice Wind Farm.

ID	Name	Contour range	
		Latitude (˚)	Longitude (˚)
1	BE-A5	58.207460 ~ 58.208031	-3.000569 ~ -2.999290
2	BE-B5	58.211030 ~ 58.211885	-2.981578 ~ -2.980660
3	BE-B6	58.221224 ~ 58.222174	-2.978122 ~ -2.977020
4	BE-B7	58.231744 ~ 58.232314	-2.974534 ~ -2.973620
5	BE-C4	58.204843 ~ 58.205699	-2.965634 ~ -2.964900
6	BE-C5	58.214703 ~ 58.215273	-2.962874 ~ -2.961770
7	BE-C6	58.224819 ~ 58.225864	-2.959245 ~ -2.958510
8	BE-C7	58.235387 ~ 58.236169	-2.956113 ~ -2.955030
9	BE-C8	58.245478 ~ 58.246537	-2.952631 ~ -2.951360
10	BE-C9	58.256084 ~ 58.256758	-2.949109 ~ -2.947837
11	BE-D3	58.199796 ~ 58.200367	-2.950213 ~ -2.949110
12	BE-D4	58.207666 ~ 58.208522	-2.947727 ~ -2.946630
13	BE-D5	58.218326 ~ 58.218802	-2.944259 ~ -2.943160
14	BE-D6	58.228702 ~ 58.229178	-2.940825 ~ -2.939730
15	BE-D7	58.239113 ~ 58.239684	-2.937332 ~ -2.936230
16	BE-D8	58.249020 ~ 58.249876	-2.933631 ~ -2.932720
17	BE-D9	58.259423 ~ 58.260278	-2.930127 ~ -2.929210
18	BE-D10	58.269745 ~ 58.270694	-2.926910 ~ -2.925810
19	BE-D11	58.280369 ~ 58.281223	-2.923460 ~ -2.922180

20	BE-E1	58.181317 ~ 58.181983	-2.937536 ~ -2.936620
21	BE-E2	58.190672 ~ 58.191433	-2.935980 ~ -2.934880
22	BE-E3	58.201174 ~ 58.201840	-2.932543 ~ -2.931440
23	BE-E4	58.211440 ~ 58.212296	-2.929087 ~ -2.927990
24	BE-E5	58.221853 ~ 58.222803	-2.925628 ~ -2.924530
25	BE-E6	58.232533 ~ 58.233009	-2.922028 ~ -2.921110
26	BE-E7	58.242821 ~ 58.243297	-2.918525 ~ -2.917430
27	BE-E8	58.252588 ~ 58.253443	-2.914995 ~ -2.913900
28	BE-E9	58.263371 ~ 58.264225	-2.911519 ~ -2.910790
29	BE-E10	58.273538 ~ 58.274395	-2.908059 ~ -2.906960
30	BE-E11	58.283805 ~ 58.284659	-2.904636 ~ -2.903540
31	BE-E12	58.294209 ~ 58.295063	-2.900994 ~ -2.900080
32	BE-F2	58.194289 ~ 58.195050	-2.917130 ~ -2.916030
33	BE-F3	58.204637 ~ 58.205304	-2.913729 ~ -2.912630
34	BE-F4	58.214986 ~ 58.215842	-2.910328 ~ -2.909230
35	BE-F5	58.225357 ~ 58.226118	-2.906831 ~ -2.905730
36	BE-F6	58.235478 ~ 58.236239	-2.903344 ~ -2.902250
37	BE-F9	58.266761 ~ 58.267426	-2.892921 ~ -2.891640
38	BE-F10	58.277177 ~ 58.277936	-2.889390 ~ -2.888290
39	BE-F11	58.287406 ~ 58.288260	-2.885635 ~ -2.884720
40	BE-F12	58.297776 ~ 58.298641	-2.882294 ~ -2.881204
41	BE-F13	58.307998 ~ 58.308757	-2.878623 ~ -2.877723
42	BE-G3	58.208901 ~ 58.209472	-2.896514 ~ -2.895420
43	BE-G4	58.218492 ~ 58.219253	-2.891590 ~ -2.890490
44	BE-G5	58.228839 ~ 58.229505	-2.887927 ~ -2.886830
45	BE-G6	58.239224 ~ 58.240080	-2.884585 ~ -2.883300
46	BE-G8	58.260057 ~ 58.260722	-2.877611 ~ -2.876700
47	BE-G9	58.270526 ~ 58.271001	-2.874122 ~ -2.873020
48	BE-G10	58.280442 ~ 58.281297	-2.870293 ~ -2.869560
49	BE-G11	58.290830 ~ 58.291684	-2.867043 ~ -2.865940
50	BE-G12	58.301341 ~ 58.301911	-2.863427 ~ -2.862526

51	BE-G13	58.311696 ~ 58.312266	-2.860128 ~ -2.858867
52	BE-G14	58.322007 ~ 58.322766	-2.856352 ~ -2.855440
53	BE-H4	58.222080 ~ 58.222841	-2.872799 ~ -2.871700
54	BE-H5	58.232499 ~ 58.233260	-2.869480 ~ -2.868200
55	BE-H6	58.242762 ~ 58.243617	-2.865922 ~ -2.864640
56	BE-H7	58.253241 ~ 58.254096	-2.862160 ~ -2.861240
57	BE-H8	58.263528 ~ 58.264098	-2.858706 ~ -2.857610
58	BE-H9	58.273963 ~ 58.274533	-2.855284 ~ -2.854190
59	BE-H10	58.284289 ~ 58.285143	-2.851824 ~ -2.850730
60	BE-H11	58.294711 ~ 58.295660	-2.847944 ~ -2.847210
61	BE-H12	58.304765 ~ 58.305524	-2.844549 ~ -2.843820
62	BE-H13	58.315179 ~ 58.316033	-2.841262 ~ -2.840160
63	BE-J5	58.236053 ~ 58.236909	-2.850483 ~ -2.849570
64	BE-J6	58.246465 ~ 58.247225	-2.847071 ~ -2.845970
65	BE-J7	58.256603 ~ 58.257470	--2.843554 ~ -2.842827
66	BE-J8	58.267188 ~ 58.268137	-2.839682 ~ -2.838950
67	BE-J9	58.277369 ~ 58.278223	-2.836433 ~ -2.835880
68	BE-J10	58.287959 ~ 58.288528	-2.832998 ~ -2.831900
69	BE-J11	58.298131 ~ 58.298890	-2.829351 ~ -2.828620
70	BE-J12	58.308436 ~ 58.309099	-2.825930 ~ -2.824830
71	BE-J13	58.318897 ~ 58.319466	-2.822632 ~ -2.821350
72	BE-K6	58.249875 ~ 58.250635	-2.828074 ~ -2.827340
73	BE-K7	58.260172 ~ 58.260932	-2.824808 ~ -2.823710
74	BE-K8	58.270840 ~ 58.271410	-2.821235 ~ -2.820140
75	BE-K9	58.281094 ~ 58.281853	-2.817787 ~ -2.816690
76	BE-K10	58.291127 ~ 58.291887	-2.814041 ~ -2.813120
77	BE-K11	58.301673 ~ 58.302338	-2.810765 ~ -2.809670
78	BE-K12	58.312337 ~ 58.312811	-2.807310 ~ -2.805850
79	BE-L7	58.263993 ~ 58.264659	-2.806043 ~ -2.804940
80	BE-L8	58.274313 ~ 58.274788	-2.802514 ~ -2.801420
81	BE-L9	58.284883 ~ 58.285547	-2.799103 ~ -2.797820

82	BE-L10	58.294803 ~ 58.295562	-2.795514 ~ -2.794420
83	BE-M9	58.288175 ~ 58.288839	-2.780312 ~ -2.779210
84	BE-M10	58.298365 ~ 58.299029	-2.776723 ~ -2.775440
85	Wind turbine A	58.099998 ~ 58.100784	-3.082761 ~ -3.081860
86	Wind turbine B	58.095349 ~ 58.096018	-3.074256 ~ -3.072790
87	BE-F8*	58.256559 ~ 58.256940	-2.896245 ~ -2.895150
88	BE-G7*	58.249683 ~ 58.250159	-2.880904 ~ -2.880170

* Offshore transformer modules (OTMs)

Table S9. The detected contour range results in Moray East Wind Farm.

ID	Name	Contour range	
		Latitude (˚)	Longitude (˚)
1	ME-A01	58.075480 ~ 58.076050	-2.870150 ~ -2.867980
2	ME-A02	58.085440 ~ 58.086600	-2.869630 ~ -2.868530
3	ME-B02	58.085470 ~ 58.086050	-2.843740 ~ -2.841760
4	ME-B03	58.095570 ~ 58.096640	-2.843090 ~ -2.842370
5	ME-B04	58.105670 ~ 58.106350	-2.843540 ~ -2.841560
6	ME-B05	58.115430 ~ 58.116400	-2.842930 ~ -2.842030
7	ME-B13	58.196800~ 58.197860	-2.843400 ~ -2.841760
8	ME-B14	58.207050 ~ 58.207530	-2.842750 ~ -2.841100
9	ME-C02	58.085320 ~ 58.085800	-2.817630 ~ -2.815820
10	ME-C04	58.105540 ~ 58.106410	-2.817080 ~ -2.816000
11	ME-C05	58.115460 ~ 58.116620	-2.817100 ~ -2.816010
12	ME-C07	58.135760 ~ 58.136920	-2.816490 ~ -2.815410
13	ME-C08	58.145800 ~ 58.146960	-2.816440 ~ -2.815340
14	ME-C09	58.155860 ~ 58.156920	-2.816520 ~ -2.815240
15	ME-C10	58.166340 ~ 58.167020	-2.817370 ~ -2.815540
16	ME-C11	58.176500 ~ 58.177080	-2.817070 ~ -2.815080
17	ME-C12	58.186740 ~ 58.187220	-2.817050 ~ -2.815420

18	ME-C13	58.196870 ~ 58.197260	-2.817410 ~ -2.815210
19	ME-C14	58.207050 ~ 58.207430	-2.817200 ~ -2.815190
20	ME-C15	58.217170 ~ 58.217550	-2.816900 ~ -2.815070
21	ME-C16	58.227250 ~ 58.227730	-2.816640 ~ -2.814990
22	ME-D04	58.105390 ~ 58.106250	-2.790640 ~ -2.789740
23	ME-D05	58.115510 ~ 58.116090	-2.791060 ~ -2.789620
24	ME-D06	58.125650 ~ 58.126610	-2.790590 ~ -2.789510
25	ME-D07	58.135640 ~ 58.136500	-2.791110 ~ -2.788940
26	ME-D08	58.145940 ~ 58.146420	-2.790880 ~ -2.789260
27	ME-D09	58.155990 ~ 58.156660	-2.790910 ~ -2.788920
28	ME-D10	58.166150 ~ 58.166730	-2.790760 ~ -2.788780
29	ME-D11	58.176150 ~ 58.176910	-2.790570 ~ -2.788940
30	ME-D12	58.186130 ~ 58.187280	-2.790700 ~ -2.789430
31	ME-D13	58.196190 ~ 58.197330	-2.789900 ~ -2.788640
32	ME-D14	58.206620 ~ 58.207480	-2.790070 ~ -2.788810
33	ME-D15	58.216690 ~ 58.217360	-2.789940 ~ -2.788660
34	ME-D16	58.226900 ~ 58.227670	-2.790000 ~ -2.788720
35	ME-D17	58.236950 ~ 58.237610	-2.789650 ~ -2.788930
36	ME-E04	58.104890 ~ 58.105950	-2.764230 ~ -2.763140
37	ME-E05	58.114890 ~ 58.115760	-2.763970 ~ -2.763240
38	ME-E14	58.206550 ~ 58.207040	-2.764210 ~ -2.762410
39	ME-E18	58.247160 ~ 58.247550	-2.763740 ~ -2.762120
40	ME-E19	58.257280 ~ 58.257760	-2.764230 ~ -2.761880
41	ME-F04	58.104970 ~ 58.105740	-2.738190 ~ -2.737100
42	ME-F08	58.145410 ~ 58.146090	-2.738260 ~ -2.736450
43	ME-F21	58.277280 ~ 58.277670	-2.737420 ~ -2.735980
44	ME-G05	58.114570 ~ 58.115530	-2.711550 ~ -2.710460
45	ME-G06	58.124970 ~ 58.125830	-2.711860 ~ -2.710780
46	ME-G07	58.134910 ~ 58.135970	-2.711500 ~ -2.710240
47	ME-G08	58.145150 ~ 58.145820	-2.712240 ~ -2.710080
48	ME-G09	58.155210 ~ 58.156080	-2.711380 ~ -2.710280

49	ME-G10	58.165380 ~ 58.166430	-2.711430 ~ -2.710170
50	ME-G11	58.175360 ~ 58.176500	-2.711170 ~ -2.710080
51	ME-G13	58.195710 ~ 58.196670	-2.711200 ~ -2.709930
52	ME-G15	58.216130 ~ 58.216710	-2.711400 ~ -2.709600
53	ME-G16	58.226490 ~ 58.226880	-2.711400 ~ -2.709230
54	ME-G17	58.236350 ~ 58.237030	-2.711540 ~ -2.709740
55	ME-G18	58.246420 ~ 58.247380	-2.710560 ~ -2.709480
56	ME-G19	58.256600 ~ 58.257360	-2.710660 ~ -2.709210
57	ME-G20	58.266680 ~ 58.267720	-2.710720 ~ -2.709090
58	ME-G21	58.277010 ~ 58.277780	-2.710630 ~ -2.709370
59	ME-G22	58.286960 ~ 58.287830	-2.710450 ~ -2.709010
60	ME-H05	58.114800 ~ 58.115190	-2.685670 ~ -2.683680
61	ME-H06	58.124520 ~ 58.125580	-2.685670 ~ -2.684230
62	ME-H07	58.134790 ~ 58.135750	-2.685630 ~ -2.684370
63	ME-H08	58.144780 ~ 58.145740	-2.685060 ~ -2.683980
64	ME-H09	58.155020 ~ 58.155790	-2.684980 ~ -2.683880
65	ME-H10	58.165030 ~ 58.165890	-2.685170 ~ -2.683730
66	ME-H11	58.175210 ~ 58.176170	-2.685050 ~ -2.683790
67	ME-H13	58.195680 ~ 58.196550	-2.684730 ~ -2.683650
68	ME-H14	58.205970 ~ 58.206830	-2.684470 ~ -2.683750
69	ME-H16	58.226130 ~ 58.226610	-2.685300 ~ -2.683310
70	ME-H17	58.235940 ~ 58.237000	-2.684250 ~ -2.683350
71	ME-H18	58.246130 ~ 58.246990	-2.684530 ~ -2.683080
72	ME-H19	58.256430 ~ 58.257290	-2.684150 ~ -2.682890
73	ME-H20	58.266850 ~ 58.267230	-2.684840 ~ -2.682640
74	ME-H21	58.276700 ~ 58.277460	-2.684520 ~ -2.682710
75	ME-H22	58.286880 ~ 58.287450	-2.684170 ~ -2.682540
76	ME-I06	58.124640 ~ 58.125510	-2.659180 ~ -2.658280
77	ME-I07	58.134450 ~ 58.135510	-2.659020 ~ -2.657750
78	ME-I18	58.245870 ~ 58.247020	-2.657780 ~ -2.656870
79	ME-I19	58.256280 ~ 58.256960	-2.657830 ~ -2.656550

80	ME-I20	58.266430 ~ 58.267110	-2.657900 ~ -2.656820
81	ME-J07	58.134320 ~ 58.135280	-2.632820 ~ -2.631550
82	ME-J08	58.144710 ~ 58.145470	-2.632900 ~ -2.631820
83	ME-J09	58.154540 ~ 58.155590	-2.632660 ~ -2.631580
84	ME-J10	58.164910 ~ 58.165490	-2.632540 ~ -2.630550
85	ME-J12	58.184860 ~ 58.185720	-2.632100 ~ -2.631020
86	ME-J13	58.194980 ~ 58.196030	-2.631910 ~ -2.631010
87	ME-J14	58.205360 ~ 58.206320	-2.632260 ~ -2.631170
88	ME-J16	58.225450 ~ 58.226410	-2.631830 ~ -2.630930
89	ME-J17	58.235790 ~ 58.236940	-2.631920 ~ -2.630840
90	ME-J18	58.245860 ~ 58.246820	-2.632270 ~ -2.630640
91	ME-J19	58.255970 ~ 58.256840	-2.631800 ~ -2.630710
92	ME-K09	58.154250 ~ 58.155300	-2.606410 ~ -2.605330
93	ME-K10	58.164300 ~ 58.165260	-2.605940 ~ -2.604860
94	ME-K11	58.174760 ~ 58.175430	-2.606570 ~ -2.604940
95	ME-K16	58.225500 ~ 58.226170	-2.606110 ~ -2.604380
96	ME-K17	58.235830 ~ 58.236600	-2.602440 ~ -2.601360
97	ME-L09	58.154090 ~ 58.154960	-2.580060 ~ -2.578980
98	ME-L11	58.174680 ~ 58.175250	-2.580260 ~ -2.578280
99	ME-L12	58.184670 ~ 58.185150	-2.579980 ~ -2.578180
100	ME-L13	58.194600 ~ 58.195650	-2.579790 ~ -2.578530
101	OSP1*	58.125490 ~ 58.125870	-2.764110 ~ -2.763390
102	OSP2*	58.216400 ~ 58.216970	-2.737380 ~ -2.736480
103	OSP3*	58.165220 ~ 58.165600	-2.658650 ~ -2.657930

* Offshore Substation Platform (OSP)

Table S10. The detected contour range results in HyWind Wind Farm (Aberdeenshire).

ID	Name	Contour range	
		Latitude (˚)	Longitude (˚)

1	HS1	57.483710 ~ 57.484580	-1.333010 ~ -1.331930
2	HS2	57.490105 ~ 57.490989	-1.352627 ~ -1.351338
3	HS3	57.496672 ~ 57.497458	-1.372470 ~ -1.371181
4	HS4	57.477897 ~ 57.478684	-1.353303 ~ -1.352034
5	HS5	57.484250 ~ 57.485321	-1.373062 ~ -1.371802

Table S11. The detected contour range results in Kincardine Wind Farm (Aberdeenshire).

ID	Name	Contour range	
		Latitude (˚)	Longitude (˚)
1	KIN-01	57.004740 ~ 57.005730	-1.882010 ~ -1.880730
2	KIN-02	56.996640 ~ 56.997340	-1.874750 ~ -1.873110
3	KIN-03	56.988690 ~ 56.989590	-1.867260 ~ -1.865980
4	KIN-04	57.018040 ~ 57.018940	-1.856110 ~ -1.854830
5	KIN-05	57.009990 ~ 57.010790	-1.848490 ~ -1.846840

Table S12. The detected contour range results in Aberdeen Offshore Wind Farm.

ID	Name	Contour range	
		Latitude (˚)	Longitude (˚)
1	AWF01	57.223170 ~ 57.223970	-2.013430 ~ -2.012170
2	AWF02	57.228119 ~ 57.228918	-2.002626 ~ -2.001718
3	AWF03	57.233165 ~ 57.234056	-1.989992 ~ -1.988723
4	AWF04	57.239830 ~ 57.240520	-1.976230 ~ -1.974950
5	AWF05	57.215390 ~ 57.216280	-2.011910 ~ -2.010820
6	AWF06	57.219750 ~ 57.220440	-2.001110 ~ -1.999460
7	AWF07	57.223890 ~ 57.224784	-1.988600 ~ -1.987330
8	AWF08	57.229623 ~ 57.230613	-1.974905 ~ -1.973817
9	AWF09	57.207500 ~ 57.208195	-2.011340 ~ -2.009520

10	AWF10	57.211302 ~ 57.212194	-1.999313 ~ -1.998024
11	AWF11	57.215623 ~ 57.216514	-1.986536 ~ -1.985083

Table S13. The topside area estimate accuracies of oil/gas platforms and semi-permanent objects in Scottish waters.

ID	Name	The detected size (Square meters)	The actual size (Square meters)	Size error (Square meters)
1	Dunbar	4100	4428	328
2	Magnus	9000	8532	468
3	Western Isles FPSO	6400	6460	60
4	Tern	4600	4950	350
5	Heather Alpha	4100	4290	190
6	Cormorant Alpha	7700	6984	716
7	North Cormorant	4400	4600	200
8	Eider	3200	3818	618
9	Ninian north *	—	—	—
10	Ninian South	6700	7199	499
11	Northern Producer *	—	—	—
12	Ninian Central	9200	8840	360
13	Thistle Alpha	6500	6460	40
14	Dunlin Alpha	7100	6840	260
15	Brent Bravo *	—	—	—
16	Brent Charlie	8100	7878	222
17	Alwyn North Bravo	3700	3551	149
18	Alwyn North Alpha	4000	3927	73
19	Brent Delta *	—	—	—
20	Noble Lloyd Noble	5200	4728	472
21	Mariner production, drilling and living quarters (PDQ)	10200	10295	95

22	Mariner floating storage unit (FSU)	10200	10130	70
23	Kraken FPSO	9600	12502	2902
24	Beryl Bravo	4400	4689	289
25	Harding	5500	5304	196
26	Beryl Alpha	1700	1406	294
27	Beryl Flare †	—	378	—
28	Beryl Alpha Riser	6800	6935	135
29	Beryl Single Point Mooring (SPM)-3	1100	1364	264
30	Beryl Single Point Mooring (SPM)-2	2100	2179	79
31	Gryphon Alpha FPSO	9800	10500	700
32	Bruce Process, Utilities and Quarters (PUQ)	4700	4698	2
33	Bruce Compression Reception (CR) †	800	706	94
34	Bruce Drilling	2300	1890	410
35	Tartan Alpha	4100	4042	58
36	Scott Drilling and Process (DP)	3100	3080	20
37	Scott Utilities and Quarters (UQ).	4400	3968	432
38	Piper Bravo	6800	6090	710
39	Saltire	3800	3726	74
40	Global Producer III FPSO	8600	8660	60
41	Alba FPSO	4300	9089	4789
42	Alba North	4200	4080	120
43	Balmoral FPSO	5800	5010	790
44	Britannia	6100	6032	68
45	Britannia Bridge-Linked Platform (BLP)	2500	2279	221
46	Hummingbird FPSO	4800	4154	646
47	Tiffany	4500	4988	488
48	Brae Alpha	4800	5427	627
49	Brae Bravo	4000	4140	140
50	Andrew	4000	4264	264
51	Brae East	3800	4088	288
52	Glen Lyon FPSO	14500	13993	507

53	Solan	2200	1856	344
54	Aoka Mizu FPSO	10000	9945	55
55	Clair	6800	6627	173
56	Clair Ridge DP	6300	5972	328
57	Clair Ridge quarters and utilities (QU)	5300	5151	149
58	Foinaven FPSO	8400	8800	400
59	Claymore Production	3300	3127	173
60	Claymore Accommodation	3000	2546	454
61	Captain BLP	2200	2236	36
62	Captain wellhead protection platform (WPP)	3900	3927	27
63	Captain FPSO	8000	7562	438
64	Ross FPSO	9200	9009	191
65	Well Head	2500	2583	83
66	Production Jacket	3300	3440	140
67	Quarters Utilities (QU) Jacket	3600	3502	98
68	Oil Stripper platform (PS)	2100	2107	7
69	Golden Eagle Wellhead	2000	2695	695
70	Golden Eagle PUQ	3400	4059	659
71	Kittiwake	3400	3832	432
72	Catcher FPSO	9000	11050	2050
73	Forties Unity	2200	1815	385
74	Anasuria FPSO	9100	9072	28
75	Forties Charlie	6100	5760	340
76	Triton FPSO	8600	9460	860
77	Forties Delta	6400	6083	317
78	Forties Bravo	4500	4180	320
79	Forties Alpha	5900	5616	284
80	Fasp	3400	3036	364
81	Gannet Alpha	4200	4158	42
82	Forties Echo	2400	2132	268
83	Nelson	5500	5346	154

84	Arbroath	2700	2304	396
85	Montrose BLP	2600	2916	316
86	Montrose Alpha	4200	4104	96
87	Etap processing, drilling and riser (PDR)	2300	2666	366
88	Etap QU	3200	3256	56
89	North Everest	3800	3440	360
90	Cats Riser	1400	1122	278
91	West Franklin wellhead platform (WHP)	2500	2352	148
92	Elgin A WHP †	1900	1890	10
93	Elgin B WHP †	6700	6561	139
94	Elgin PUQ	2200	3129	929
95	Franklin WHP	6900	6520	380
96	Culzean Utilities and Living Quarters (ULQ)	2800	2960	160
97	Culzean Central Processing Facility (CPF)	2900	3042	142
98	Culzean WHP	6100	5920	180
99	Shearwater A	4500	4860	360
100	Shearwater C	3700	3564	136
101	Erskine	2300	2028	272
102	FPF1 FPSO	6800	6525	275
103	Mungo	2200	2090	110
104	Lomond	3600	3276	324
105	Jasmine Wellhead	7400	7112	288
106	Jasmine Living Quarters (JLQ)	2200	2180	20
107	Jade	2300	2108	192
108	Haewene Brim FPSO	4500	6534	2034
109	Judy Riser and Separation Platform (JRP)	4000	4176	176
110	Judy	5500	5775	275
111	Culzean FSO - Ailsa	5000	8697	3697
112	Armada	4200	4699	499
113	Jacky platform	5500	5102	398
114	Beatrice Charlie *	—	—	—

115	Betrice Alpha Drilling *	—	—	—
116	Beatrice Alpha Production *	—	—	—
117	Beatrice Bravo *	—	—	—
118	Manifold and Compression Platform 01 (MCP01) *	—	—	—
119	Frigg Treatment platform 1 (TP1) *	—	—	—
120	Frigg Concrete drilling platform 1 (CDP1) *	—	—	—
121	Frigg Treatment Compression Platform 2 (TCP 2) *	—	—	—

* The infrastructure has undergone decommissioning.

† The infrastructure is omitted in Sentinel-2 data.

Table S14. The diameter length estimate accuracies of wind turbines in Beatrice Wind Farm.

ID	Name	The detected size (meter)	The actual size (meter)	The size error (meter)
1	BE-A5	160±5	154	6±5
2	BE-B5	145±5	154	9±5
3	BE-B6	145±5	154	9±5
4	BE-B7	135±5	154	19±5
5	BE-C4	160±5	154	6±5
6	BE-C5	145±5	154	9±5
7	BE-C6	150±5	154	4±5
8	BE-C7	135±5	154	19±5
9	BE-C8	160±5	154	6±5
10	BE-C9	140±5	154	14±5
11	BE-D3	135±5	154	19±5
12	BE-D4	160±5	154	6±5
13	BE-D5	150±5	154	4±5
14	BE-D6	170±5	154	16±5
15	BE-D7	145±5	154	9±5
16	BE-D8	160±5	154	6±5
17	BE-D9	165±5	154	11±5
18	BE-D10	170±5	154	16±5

19	BE-D11	160±5	154	6±5
20	BE-E1	155±5	154	1±5
21	BE-E2	145±5	154	9±5
22	BE-E3	150±5	154	4±5
23	BE-E4	145±5	154	9±5
24	BE-E5	170±5	154	16±5
25	BE-E6	145±5	154	9±5
26	BE-E7	135±5	154	19±5
27	BE-E8	160±5	154	6±5
28	BE-E9	170±5	154	16±5
29	BE-E10	155±5	154	1±5
30	BE-E11	155±5	154	1±5
31	BE-E12	145±5	154	9±5
32	BE-F2	135±5	154	19±5
33	BE-F3	145±5	154	9±5
34	BE-F4	145±5	154	9±5
35	BE-F5	135±5	154	19±5
36	BE-F6	145±5	154	9±5
37	BE-F9	145±5	154	9±5
38	BE-F10	140±5	154	14±5
39	BE-F11	140±5	154	14±5
40	BE-F12	155±5	154	1±5
41	BE-F13	150±5	154	4±5
42	BE-G3	145±5	154	9±5
43	BE-G4	145±5	154	9±5
44	BE-G5	135±5	154	19±5
45	BE-G6	145±5	154	9±5
46	BE-G8	155±5	154	1±5
47	BE-G9	145±5	154	9±5
48	BE-G10	170±5	154	16±5

49	BE-G11	170±5	154	16±5
50	BE-G12	135±5	154	19±5
51	BE-G13	155±5	154	1±5
52	BE-G14	145±5	154	9±5
53	BE-H4	170±5	154	16±5
54	BE-H5	155±5	154	1±5
55	BE-H6	160±5	154	6±5
56	BE-H7	150±5	154	4±5
57	BE-H8	155±5	154	1±5
58	BE-H9	135±5	154	19±5
59	BE-H10	145±5	154	9±5
60	BE-H11	150±5	154	4±5
61	BE-H12	150±5	154	4±5
62	BE-H13	140±5	154	14±5
63	BE-J5	140±5	154	14±5
64	BE-J6	135±5	154	19±5
65	BE-J7	150±5	154	4±5
66	BE-J8	150±5	154	4±5
67	BE-J9	140±5	154	14±5
68	BE-J10	160±5	154	6±5
69	BE-J11	150±5	154	4±5
70	BE-J12	135±5	154	19±5
71	BE-J13	150±5	154	4±5
72	BE-K6	170±5	154	16±5
73	BE-K7	145±5	154	9±5
74	BE-K8	140±5	154	14±5
75	BE-K9	140±5	154	14±5
76	BE-K10	150±5	154	4±5
77	BE-K11	145±5	154	9±5
78	BE-K12	145±5	154	9±5

79	BE-L7	135±5	154	19±5
80	BE-L8	135±5	154	19±5
81	BE-L9	170±5	154	16±5
82	BE-L10	155±5	154	1±5
83	BE-M9	145±5	154	9±5
84	BE-M10	145±5	154	9±5
85	Wind turbine A	145±5	154	9±5
86	Wind turbine B	155±5	154	1±5
87	BE-F8*	—	—	—
88	BE-G7*	—	—	—

* Offshore transformer modules (OTMs)

Table S15. The diameter length estimate accuracies in Moray East Wind Farm.

ID	Name	The detected size (meter)	The actual size (meter)	The size error (meter)
1	ME-A01	160±5	164	4±5
2	ME-A02	170±5	164	6±5
3	ME-B02	160±5	164	4±5
4	ME-B03	145±5	164	19±5
5	ME-B04	180±5	164	16±5
6	ME-B05	180±5	164	16±5
7	ME-B13	185±5	164	21±5
8	ME-B14	160±5	164	4±5
9	ME-C02	165±5	164	1±5
10	ME-C04	150±5	164	14±5
11	ME-C05	170±5	164	6±5
12	ME-C07	170±5	164	6±5
13	ME-C08	170±5	164	6±5
14	ME-C09	180±5	164	16±5

15	ME-C10	155±5	164	9±5
16	ME-C11	155±5	164	9±5
17	ME-C12	145±5	164	19±5
18	ME-C13	160±5	164	4±5
19	ME-C14	160±5	164	4±5
20	ME-C15	150±5	164	14±5
21	ME-C16	150±5	164	14±5
22	ME-D04	150±5	164	14±5
23	ME-D05	145±5	164	19±5
24	ME-D06	170±5	164	6±5
25	ME-D07	185±5	164	21±5
26	ME-D08	150±5	164	14±5
27	ME-D09	160±5	164	4±5
28	ME-D10	160±5	164	4±5
29	ME-D11	155±5	164	9±5
30	ME-D12	185±5	164	21±5
31	ME-D13	170±5	164	6±5
32	ME-D14	145±5	164	19±5
33	ME-D15	150±5	164	14±5
34	ME-D16	145±5	164	19±5
35	ME-D17	140±5	164	24±5
36	ME-E04	170±5	164	6±5
37	ME-E05	170±5	164	6±5
38	ME-E14	145±5	164	19±5
39	ME-E18	145±5	164	19±5
40	ME-E19	180±5	164	16±5
41	ME-F04	145±5	164	19±5
42	ME-F08	155±5	164	9±5
43	ME-F21	145±5	164	19±5
44	ME-G05	170±5	164	6±5

45	ME-G06	150±5	164	14±5
46	ME-G07	170±5	164	6±5
47	ME-G08	170±5	164	6±5
48	ME-G09	150±5	164	14±5
49	ME-G10	180±5	164	16±5
50	ME-G11	170±5	164	6±5
51	ME-G13	155±5	164	9±5
52	ME-G15	155±5	164	9±5
53	ME-G16	170±5	164	6±5
54	ME-G17	170±5	164	6±5
55	ME-G18	160±5	164	4±5
56	ME-G19	150±5	164	14±5
57	ME-G20	185±5	164	21±5
58	ME-G21	145±5	164	19±5
59	ME-G22	170±5	164	6±5
60	ME-H05	170±5	164	6±5
61	ME-H06	170±5	164	6±5
62	ME-H07	155±5	164	9±5
63	ME-H08	150±5	164	14±5
64	ME-H09	150±5	164	14±5
65	ME-H10	185±5	164	21±5
66	ME-H11	155±5	164	9±5
67	ME-H13	145±5	164	19±5
68	ME-H14	180±5	164	16±5
69	ME-H16	180±5	164	16±5
70	ME-H17	180±5	164	16±5
71	ME-H18	170±5	164	6±5
72	ME-H19	155±5	164	9±5
73	ME-H20	170±5	164	6±5
74	ME-H21	155±5	164	9±5

75	ME-H22	150±5	164	14±5
76	ME-I06	150±5	164	14±5
77	ME-I07	160±5	164	4±5
78	ME-I18	170±5	164	6±5
79	ME-I19	145±5	164	19±5
80	ME-I20	145±5	164	19±5
81	ME-J07	155±5	164	9±5
82	ME-J08	150±5	164	14±5
83	ME-J09	170±5	164	6±5
84	ME-J10	180±5	164	16±5
85	ME-J12	170±5	164	6±5
86	ME-J13	170±5	164	6±5
87	ME-J14	155±5	164	9±5
88	ME-J16	155±5	164	9±5
89	ME-J17	180±5	164	16±5
90	ME-J18	170±5	164	6±5
91	ME-J19	150±5	164	14±5
92	ME-K09	170±5	164	6±5
93	ME-K10	170±5	164	6±5
94	ME-K11	145±5	164	19±5
95	ME-K16	155±5	164	9±5
96	ME-K17	170±5	164	6±5
97	ME-L09	155±5	164	9±5
98	ME-L11	155±5	164	9±5
99	ME-L12	145±5	164	19±5
100	ME-L13	170±5	164	6±5
101	OSP1*	—	—	—
102	OSP2*	—	—	—
103	OSP3*	—	—	—

* Offshore Substation Platform (OSP)

Table S16. The diameter length estimate accuracies in HyWind Wind Farm (Aberdeenshire).

ID	Name	The detected size (meter)	The actual size (meter)	The size error (meter)
1	HS1	145±5	154	9±5
2	HS2	145±5	154	9±5
3	HS3	160±5	154	6±5
4	HS4	145±5	154	9±5
5	HS5	155±5	154	1±5

Table S17. The diameter length estimate accuracies in Kincardine Wind Farm (Aberdeenshire).

ID	Name	The detected size (meter)	The actual size (meter)	The size error (meter)
1	KIN-01	160±5	164	4±5
2	KIN-02	155±5	164	9±5
3	KIN-03	160±5	164	4±5
4	KIN-04	155±5	164	9±5
5	KIN-05	155±5	164	9±5

Table S18. The diameter length estimate accuracies in Aberdeen Offshore Wind Farm.

ID	Name	The detected size (meter)	The actual size (meter)	The size error (meter)
1	AWF01	145±5	150	5±5
2	AWF02	145±5	150	5±5
3	AWF03	155±5	150	5±5
4	AWF04	140±5	150	10±5
5	AWF05	140±5	150	10±5
6	AWF06	155±5	150	5±5
7	AWF07	145±5	150	5±5
8	AWF08	140±5	150	10±5
9	AWF09	145±5	150	5±5

10	AWF10	160±5	150	10±5
11	AWF11	155±5	150	5±5

Figures

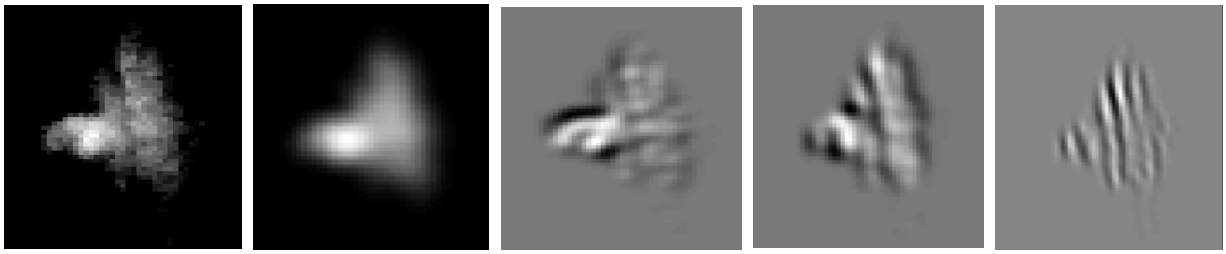

(a) (b) (c) (d) (e)

Fig. S1 The different components of the input Sentinel-1 image after 2D-SSA decomposition. (a) The input median composite image; (b) The 1st component; (c) The 2nd component; (d) The 3rd component; (e) The 4th component.

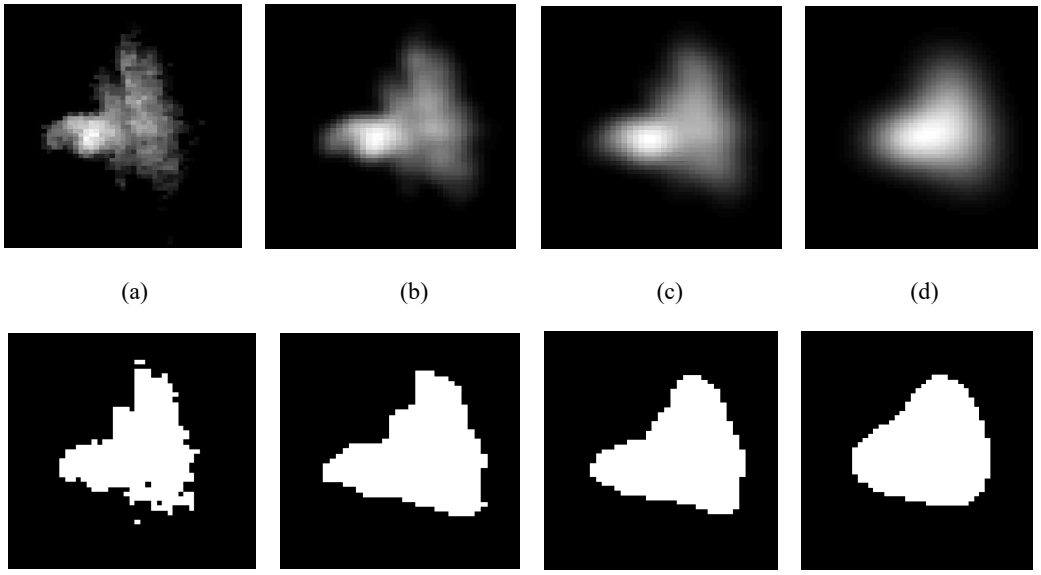

(a) (b) (c) (d)

(e) (f) (g) (h)

Fig. S2. The effects of different window sizes of 2D-SSA on the proposed method. (a) The input median composite image; (b) The filtered image by 2D-SSA with window size of 3×3; (c) The filtered image by 2D-SSA with window size of 5×5; (d) The filtered image by 2D-SSA with window size of 10×10; (e) The threshold segmentation results of (a); (f) The threshold segmentation results of (b); (g) The threshold segmentation results of (c); (h) The threshold segmentation results of (d).

When applying 2D-SSA, the image can be decomposed and reconstructed based on the eigenvalues obtained in singular value decomposition (SVD). In general, the first component contains the main information of input data, while noises are usually existed in those small eigenvalues. Fig. S1. shows the different components of input Sentinel-1 image after 2D-SSA decomposition. It is clear that the first component in Fig. S1. (b) contains the clearer and more discriminative features of the platforms, while the 2^{nd}, 3^{rd}, 4^{th} components in Fig. S1. (c)-(e) keep the noisy contents. Therefore, in this paper, we only utilize the first component to reconstruct the image.

Another key parameter in 2D-SSA is the window size, which also affects the noise level of image. A large window size leads to more smoothed results with most of noisy content removed. Here, the effects of different window sizes are test. The filtered images by 2D-SSA with the wind sizes of 3×3, 5×5, and 10×10, and their corresponding results by threshold segmentation are depicted in Fig. S2. It is clear that increasing the window size can reduce the noises in threshold segmentation result. When using the window size of 3×3, there are still some noises on the edges of the detected object as shown in Fig. S2 (f). However, when the window size equals to 10×10, the filtered image in Fig. S2 (d) would lose many feature details of object with the distorted segmentation result. Besides, a large window size in 2D-SSA would increase the computational cost. Therefore, to achieve an efficient and effective filter, the window sizes of 5×5 and the first component is employed in 2D-SSA.

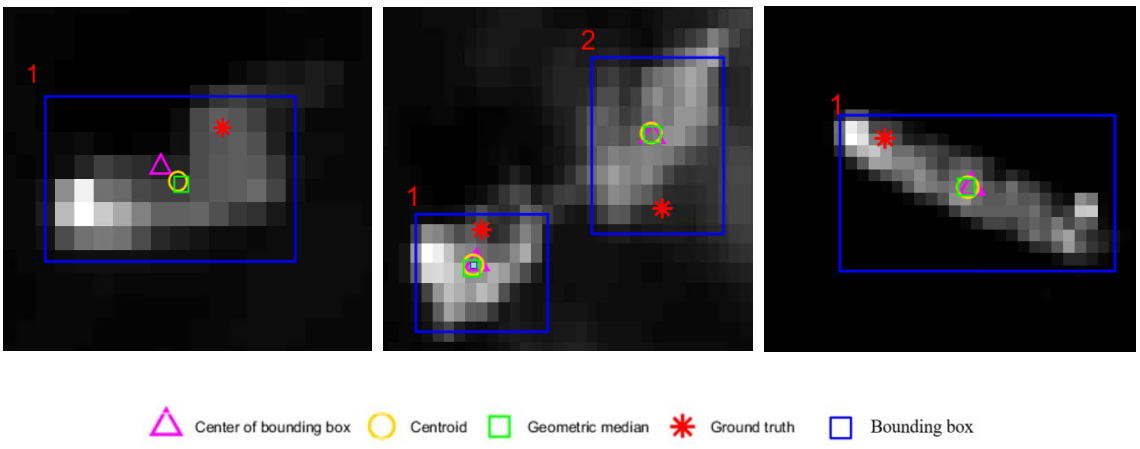

(a) (b) (c)

Fig. S3. The center location and ground truth of offshore infrastructure. (a) Clair platform; (b) The linked rig including Clair Ridge DP and Clair Ridge QU; (c) Aoka Mizu FPSO.

In this paper, an offshore infrastructure is considered as a correct identification when its ground truth is within the detected contour range. The databases used for constructing ground truth could lack up-to-date information. Fig. S3 shows the bounding box and three kinds of centers based on the detection results, and the corresponding ground truth location of different offshore infrastructure. Here the center of bounding box, centroid and geometric median are used respectively for presenting the center location of the detected infrastructure. Note that geometric median denotes the location that minimizes the sum of distances to all detected pixels of target. From Fig. S3, it is clear that the bounding box can effectively extract the contour range of each offshore infrastructure. As shown in Fig. S3, the ground truth can locate the target infrastructure but not in the exact center position. In comparison, the center of bounding box, centroid and geometric median can better locate the center location. Especially for the FPSO, such as Aoka Mizu FPSO shown in Fig. S3 (c), it would drift with wave and need updates in ground truth frequently. Given this, we use the contour range in this paper to locate the whole structure of an offshore infrastructure.